
















## Photometry, Centroid and Point-Spread Function Measurements in the LSST Camera Focal Plane Using Artificial Stars

JOHNNY H. ESTEVES <sup>1</sup>, YOUSUKE UTSUMI <sup>2,3</sup>, ADAM SNYDER <sup>4</sup>, THEO SCHUTT <sup>2,3</sup>, ALEX BROUGHTON <sup>5</sup>,  
BAHRUDIN TRBALIC<sup>2</sup>, SIDNEY MAU <sup>2</sup>, ANDREW RASMUSSEN<sup>2,3</sup>, ANDRÉS A. PLAZAS MALAGÓN <sup>2,3</sup>,  
ANDREW BRADSHAW <sup>2,3</sup>, STUART MARSHALL L. <sup>2,3</sup>, SETH DIGEL <sup>2,3</sup>, JAMES CHIANG <sup>2,3</sup>, ELI RYKOFF <sup>3</sup>,  
CHRIS WATERS <sup>6</sup>, MARCELLE SOARES-SANTOS <sup>1</sup> AND AARON ROODMAN <sup>2,3</sup>

<sup>1</sup>*Department of Physics, University of Michigan, Ann Arbor, Michigan, United States*

<sup>2</sup>*Kavli Institute for Particle Astrophysics and Cosmology, Stanford University, Stanford, California, United States*

<sup>3</sup>*SLAC National Accelerator Laboratory, Menlo Park, California, United States*

<sup>4</sup>*Department of Physics and Astronomy, University of California/Davis, Davis, California, United States*

<sup>5</sup>*Department of Physics & Astronomy, University of California/Irvine, Irvine, California, United States*

<sup>6</sup>*Department of Astrophysical Sciences, Princeton University, Princeton, New Jersey, United States*

### ABSTRACT

The Vera C. Rubin Observatory’s LSST Camera (LSSTCam) pixel response has been characterized using laboratory measurements with a grid of artificial stars. We quantify the contributions to photometry, centroid, point-spread function size, and shape measurement errors due to small anomalies in the LSSTCam CCDs. The main sources of those anomalies are quantum efficiency variations and pixel area variations induced by the amplifier segmentation boundaries and “tree-rings” — circular variations in silicon doping concentration. This laboratory study using artificial stars projected on the sensors shows overall small effects. The residual effects on point-spread function (PSF) size and shape are below 0.1%, meeting the ten-year LSST survey science requirements. However, the CCD mid-line presents distortions that can have a moderate impact on PSF measurements. This feature can be avoided by masking the affected regions. Effects of tree-rings are observed on centroids and PSFs of the artificial stars and the nature of the effect is confirmed by a study of the flat-field response. Nevertheless, further studies of the full-focal plane with stellar data should more completely probe variations and might reveal new features, e.g. wavelength-dependent effects. The results of this study can be used as a guide for the on-sky operation of LSSTCam.

*Keywords:* Rubin Observatory; Rubin Observatory Legacy Survey of Space and Time (LSST); LSST Camera; CCDs; Tree-rings; Shear

### 1. INTRODUCTION

The Vera C. Rubin Observatory is a next-generation optical and near-infrared observatory currently under construction in Cerro Pachón, Chile. The Rubin Observatory will conduct the Legacy Survey of Space and Time (LSST), an unprecedented galaxy survey of 18000 sq-deg of the southern sky that will revisit each area over 825 times in 10 years and in six photometric bands, *ugrizy*. The four science pillars of LSST main are to probe the nature of dark energy and dark matter, take an inventory of the solar system, explore the transient optical sky, and study the evolution and structure of the Milky Way (Ivezić et al. 2019). To achieve these goals, the Rubin Observatory will use the 3.2 gigapixel LSST Camera (LSSTCam), mounted on the 8.4-meter

Simonyi Survey Telescope. The LSSTCam has a large field of view of approximately 10 sq-deg, with a focal plane of 201 4k by 4k, thick (100  $\mu\text{m}$ ), fully-depleted, back-illuminated charge-coupled devices (CCDs; Holland et al. 2003, 2009, 2014).

The focal plane of the LSSTCam is populated by 189 science CCDs, 8 CCDs for auto-guiding, and 4 split CCDs for wavefront measurements. The focal plane consists of 25 sub-assemblies, 21 Science Rafts (O’Connor et al. 2016) with a 3×3 mosaic of science CCDs and 4 Corner Rafts (Arndt et al. 2010) each with two guiders and one split wavefront sensor. For LSST custom CCDs, an array of (10  $\mu\text{m}$ )<sup>2</sup> pixels with a thickness of 100  $\mu\text{m}$  back-illuminated deep-depletion devices were developed. These sensors feature 16 amplifier segments,

each 2k by 0.5k, arranged in two rows of eight segments and separated by a mid-line break, to enable low-noise, two-second readout via parallel readout of the segments. The CCD sensors were fabricated by two vendors: Imaging Technology Laboratory (ITL) and Teledyne e2v (e2v). Both vendors meet the LSST CCD requirements (Radeka et al. 2009; Doherty et al. 2014; Kovtsov et al. 2016) but there are subtle differences between those sensors.

Thick, high-resistivity CCDs have been used by other wide-field imagers such as the Dark Energy Camera (DECam, Flaugher et al. (2015a)) and the Hyper Suprime-Cam (HSC, Miyazaki et al. (2018)), in part due to their high quantum efficiency (QE) at longer wavelengths (near infrared). However, these types of detectors have been found to imprint subtle but significant undesirable characteristics that impact centroid, photometric, flux, and shape measurements (Stubbs 2014; Astier 2015; Mandelbaum 2015). Study and characterization of any source of systematic errors will be crucial to achieving the required accuracy to achieve the scientific goals of a survey such as the LSST.

An initial study characterizing prototype LSST sensors was performed to ensure that the CCDs met basic LSST performance requirements for, e.g., read noise, quantum efficiency, charge transfer efficiency, diffusion and full well (Doherty et al. 2014). Snyder et al. (2018) studied optimization of operational voltages for sensors from ITL. Snyder et al. (2021a,b) performed measurements of effects of sensor anomalies such as deferred charge distortions, centroid shifts, and the brighter-fatter effect (Gruen et al. 2015). Park et al. (2017, 2020) studied the imprints of circular patterns due to silicon dopant concentration variation (tree-rings effect) on flat-field images for the full set of LSST CCDs.

In addition, Juramy et al. (2020) studied an anomaly called “tearing”, a visually striking distortion created during the e2v readout. The distortion at the mid-line break and the amplifier boundaries is different dynamically with respect to light. The bias and clock voltages as well as the CCD controller sequence were optimized in the course of individual Raft and focal plane testing. Comprehensive results of the overall testing campaign will be described in a future publication.

This paper presents a initial assessment of sensor effects related to moments of the brightness distributions (up to second order) of star-like spots, for selected sensors. We quantify the observed anomalies in terms of the desired limits on systematic uncertainties for the LSST, paying special attention to effects occurring at certain locations on the CCDs. Effects from tree-rings are observed in the measured centroid and point-spread

function (PSF), and in flat-field response, with a consistent interpretation of the origin. Our results will be the foundation for further investigation of the sensor systematics over the full focal plane using on-sky data, and development of future corrections, if needed. However, these topics are beyond the scope of the present work.

## 2. FOCAL PLANE: SPOT GRID TEST

This section first describes the laboratory test setup and the data acquisitions, then the imaging data collection and the post-processing methodology, which includes the source detection, the grid fitting algorithm, and the calibration of the spot-measured quantities: flux, centroid, PSF shape, and size.

### 2.1. Camera Bench For Optical Testing: Spot Projector

The focal plane in the Camera cryostat was mounted on the top of the Bench for Optical Testing (BOT), facing downward. The BOT was designed to achieve a dark environment for electro-optical testing of the focal plane. The background light is reduced to below 0.01 electrons per second per pixel, an ideal environment to perform optical tests without light contamination. For a complete description of the BOT design, assembly, and requirements, see Newbry et al. (2018); Snyder et al. (2021b).

Underneath the BOT, we mounted the spot projector, which creates the artificial star grid by projecting the image of a spot mask onto the focal plane. The spot projector experimental apparatus has a 450 nm light-emitting diode (LED) light source fed by an optical fiber into the integrating sphere gated by a single-blade beam shutter (“Thorlabs 1”). The spot pattern is set by a photographic mask (HTA Photomask photolithographic) on the filter wheel. The commercial lens (Nikon 105mm f/2.8 Ai-s Micro-Nikkor) is used to re-image the integrating sphere’s 1” exit port. The F-stop ring was set to be closed as much as possible. The entire image of the mask is about the size of an LSST CCD.

The spot projector is placed on a remotely controlled XY stage. This XY stage allows the translation of the projector to point at any location of the focal plane. The spots projected onto the focal plane form a uniform, rectangular grid with  $750\ \mu\text{m}$  (75 pixel) spacing between nearest neighbors. Overall, the grid has  $49 \times 49$  spots, as shown in Figure 1.

### 2.2. Data Acquisition

We collected images for this analysis in two series, Run 3 and Run 5. We began with a randomly selected sensor from each vendor: R22-S11 (e2v) and R02-S02 (ITL).

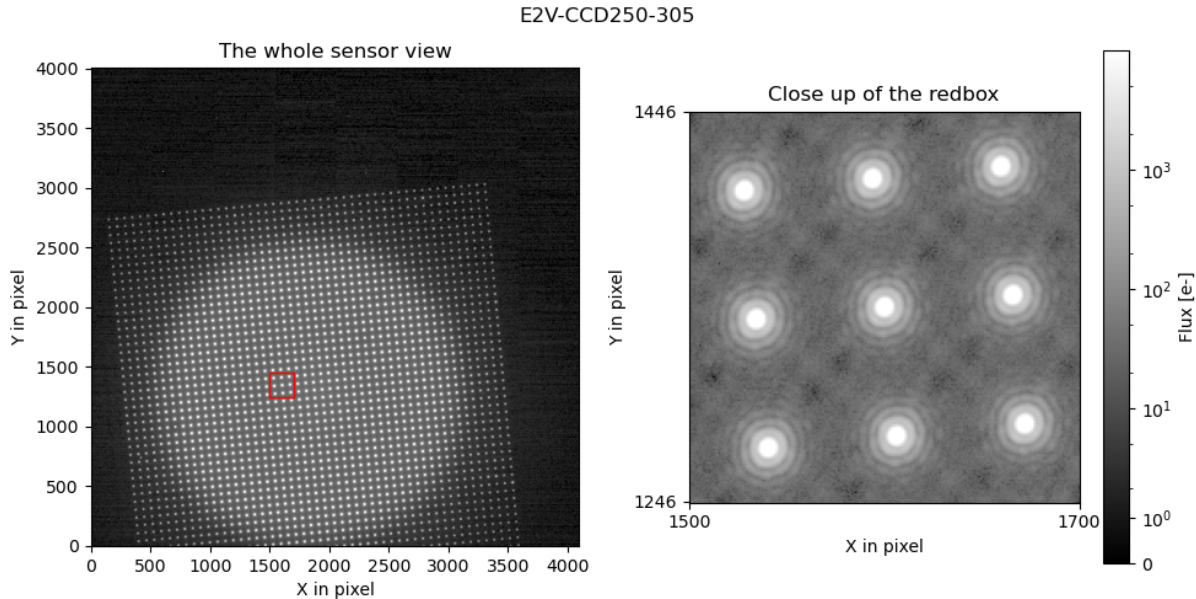


**Figure 1.** Example images of (left) the 49x49 spot grid and (right) a close up of the highlighted region on the left, respectively. The star-like spots are approximate point sources, with FWHM 5.2 pixels. The grid allow probing much of the sensor area with each acquisition. Note that the sources located in the corners are masked due to their diminished flux, a result of the vignetting effect produced by the commercial lens in our setup.

It was a pilot study during the third round of electro-optical testing campaigns at SLAC (Run 3; 2019/10/4–2019/11/5). Then we extended the scope to four additional sensors in Run 5 (2021/11/4 and 2022/1/6) with some improvements in the acquisition procedure: two ITL sensors (R03-S12, R10-S11) and two e2v sensors (R24-S11, R32-S01). The nominal flux of the spots was set at  $\sim 50000$  e-/pixel, which is bright relative to the readout noise,  $\sim 10$  e-, and well below sensor full well,  $\sim 100000$  e-. The sensor voltages readout sequence parameters are different between those two data acquisition campaigns. The specific parameters are tabulated in [Appendix A](#).

In Run 3, we collected 1600 images with the spot projector position randomly dithered around the center of each of the studied CCDs, spanning  $\pm 5$  mm in Run 3. However, we found two major technical issues with the Run 3 images: (a) the projected spot grid did not cover an entire CCD; (b) the images were not sharply focused. Therefore, in Run 5, we changed the acquisition to 2000 randomly dithered images at the center and four quadrants of the studied CCDs, spanning  $\pm 5$ mm to cover the entire CCD. [Figure 2](#) shows the dithering pattern.

For Run 5 we also replaced a manual adjustable Z-stage on the XY stage with a remotely controlled Z-stage to address the focus issue. This updated setup significantly improved the focusing process. However, the structure of the Z-stage introduced vibrations that were significant at the physical size of the projected

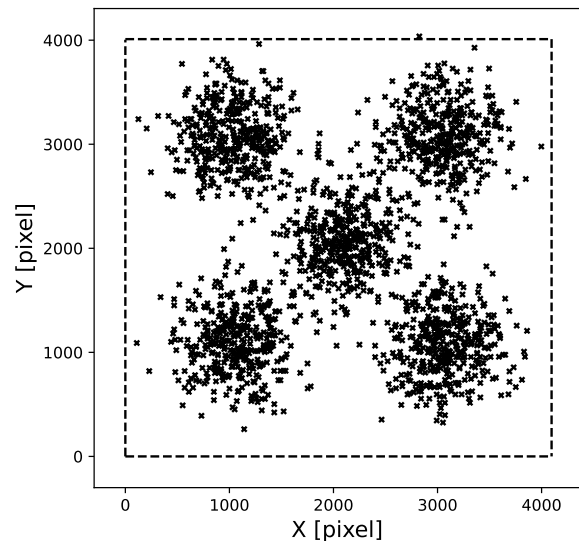


**Figure 2.** An example of the updated dithering pattern for R24-S11. The crosses represent the locations of the centers of the spot grid pattern for the 2000 acquisition. The CCD frame is outlined by the dashed lines.

spots. These effects were corrected through post processing because they were identified during data analysis after Run 5 was completed. In [Sec. 2.5](#), we describe our corrections.

### 2.3. Artificial Stars Image Collection

An example of a single exposure taken during the imaging acquisition process is shown in Figure 1. The left-hand panel illustrates our star-like field, a square grid with  $49 \times 49$  optical spots projected on the CCD. Note that the grid spans a large part of the detector in a single exposure. The star-like physical size and Gaussian shape of the spots may be discerned from the figure. The spots on the grid are equally spaced and have FWHM of  $\sim 5$  pixels, corresponding to  $\sim 1''$  in the LSSTCam focal plane. With an average ellipticity of  $\sim 0$ , the spots are quite similar to point sources, and their size was chosen to be equivalent to the PSF of the camera.

The optical setup creates image artifacts as shown in Figure 1. For instance, the commercial lens vignettes the image; the spots on the edges are affected and have significantly lower flux. In addition, the spots have a characteristic shape and size that vary across the grid. The setup design can then impact our analysis if not treated correctly. Therefore, having many exposures and different spots for each CCD pixel is desirable to mitigate effects from the experimental setup. Sec. 2.5 further describes our statistical treatment of the experimental setup imperfections.

#### 2.4. Single Image Processing And Grid Characterization

Here we describe the analysis for a single exposure, from raw image to the resulting catalog of identified sources. The spot exposures presented in Sec. 2.3 were analyzed using version 21.0.0 of the LSST Science Pipelines (hereafter pipelines; <https://pipelines.lsst.io>; Bosch et al. 2018, 2019). The pipelines is a set of data processing tasks actively being developed to process the LSST data. The raw images taken of the spot grid were processed using the standard pipelines instrument signature removal (ISR) task. An extension to the standard pipelines for these lab spot images was developed and used (`mixcoat1`). This procedure includes a bias level subtraction using the row-by-row median value of the overscan region, 2D structure in the bias using a medianed overscan-subtracted bias image, masking of pixel defects, and applying gain correction as derived from measurements using an Fe<sup>55</sup> X-ray source. To better observe sensor anomalies, we do not apply flat field corrections.

After ISR processing, the identification of sources and measurement of source properties was performed using a custom source detection task `mixcoat1.characterizeSpots.CharacterizeSpotsTask`. This task detects sources by applying a maximum filter to the image and identifying peaks above a pixel

value threshold of 200 electrons. This methodology was needed because the spatial variation of the projector’s scattered light background was ill-suited for the background modeling and subtraction performed by the standard pipelines source detection task. The detected sources’ fluxes ( $f$ ), positions ( $x, y$ ), and second moments of brightness ( $I_{xx}$ ,  $I_{xy}$ , and  $I_{yy}$ ) were measured using the SDSS HSM algorithm (Hirata & Seljak 2003; Mandelbaum et al. 2005; Bosch et al. 2018). The second moment of brightness for an object  $S(\mathbf{x})$  is given by:

$$I_{ij} = 2 \frac{\int_{\mathbf{R}^2} (\mathbf{x} - \mathbf{x}_0)_i (\mathbf{x} - \mathbf{x}_0)_j w(\mathbf{x}) S(\mathbf{x}) d^2\mathbf{x}}{\int_{\mathbf{R}^2} w(\mathbf{x}) S(\mathbf{x}) d^2\mathbf{x}}, \quad (1)$$

where  $w(\mathbf{x})$  are the weights that maximizes the S/N under the assumption of an elliptical Gaussian shape. The algorithm details can be found in Bosch et al. (2018).

The next step was to derive the properties of the projected grid from the set of detected sources, including the overall magnification, the row/column spacing, and the rotation of the grid with respect to the pixel array. We filtered the outlier sources with the following threshold  $2.0 < I_{xx}$  or  $I_{yy} < 20.0 \text{ px}^2$  in order to exclude sources that do not correspond to points on the projected grid. The remaining sources were then fit to an ideal grid model of  $49 \times 49$  spots, with three free parameters corresponding to the x/y grid center position and  $\theta$  the grid angle. We employed a least-squares minimization approach to minimize the distances between detected and grid model source positions. To initiate the grid model fitting step, we utilized a convex hull technique to provide an initial guess. The convex hull method proved to be more robust than using the commanded grid center as an initial value. After determining a best-fit model grid, each detected source was assigned an index label corresponding to its row and column number in the projected grid; this identification allowed for tracking individual sources across exposures. The per-source position residuals from the ideal grid model were then calculated and recorded in the source catalog for the measurement of optical and sensor distortions, as described in Sec. 2.5.

#### 2.5. Measurement Calibrations: Residuals

Here we describe how we calibrate our measurements.

As shown in Sec. 2.3, the spots are not ideal point sources, and their locations on the grid, shape deviations, and projector lens aberrations, for example, impact their measured quantities. In order to remove effects of the optical aberrations, we compute the residuals of a measured and ideal spot property for a large collection of exposures centered at different positions. The



residual vector  $\delta\vec{\ell}$  between the position of an ideal grid spot  $\vec{s}$  and the position of the corresponding detected spot  $\vec{d}$  is (Snyder et al. 2021b):

$$\delta\vec{\ell} = \delta\vec{\ell}_{\text{optical}} + \delta\vec{\ell}_{\text{sensor}} + \vec{\epsilon}, \quad (2)$$

where  $\vec{\epsilon}$  is a random error term,  $\delta\vec{\ell}_{\text{optical}}$  represents displacements that can be caused by the optical setup, including the mask used to generate the spots that are constant and independent of the position of the projector. If we average the residual  $\delta\vec{\ell}$  of one single spot measured at many different locations on the CCD, the sensor anomalies should average out, and only the constant displacements due to the optical setup will remain. For a sufficiently large set of residual measurements, the sensor anomalies should be:

$$\delta\vec{\ell}_{\text{sensor}} = \delta\vec{\ell} - \langle \delta\vec{\ell} \rangle, \quad (3)$$

where  $\langle \delta\vec{\ell} \rangle$  is a constant value for one spot since it is the average residual vector over the CCD pixels. For randomly distributed errors, the expectation value of the error term is zero. The statistical error can be reduced by increasing the sample size.

Similarly, the residuals of the PSF shape and size are computed in terms of the residuals of the second moments of brightness (Bernstein & Jarvis 2002):

$$\delta I_{ij} = I_{ij} - \langle I_{ij} \rangle, \quad (4)$$

The second moments of brightness are a building block for the PSF shape and size measurements (Kaiser et al. 1995; Schneider 2005):

$$T = I_{xx} + I_{yy} \quad (5)$$

$$e_1 = (I_{xx} - I_{yy})/T \quad (6)$$

$$e_2 = 2I_{xy}/T \quad (7)$$

where  $T$  is the PSF-size, and  $e_1$  and  $e_2$  are the  $x$  and  $y$  components of ellipticity. We note that others definitions of ellipticity from the second moments of brightness are possible (Schneider 2005). Also, the above definition of PSF-size ( $T$ ) relates to the PSF full width at half maximum (FWHM) as:

$$\text{FWHM} \equiv 2.355\sigma = 2.355\sqrt{T/2}, \quad (8)$$

if the profile is Gaussian.

The resulting residuals of the PSF shape and size are:

$$\delta T = \delta I_{xx} + \delta I_{yy} \quad (9)$$

$$\delta e_1 = (\delta I_{xx} - \delta I_{yy})/\langle T \rangle \quad (10)$$

$$\delta e_2 = 2\delta I_{xy}/\langle T \rangle. \quad (11)$$

We computed the fractional flux residuals in terms of the ratio:

$$\frac{\delta f}{f} = \frac{f - \langle f \rangle}{\langle f \rangle}, \quad (12)$$

For small fluxes residuals ( $\delta f/f$ ) can be expressed as a multiplicative factor, where  $\delta m \approx -1.08573\delta f/f$  mag.

For the record, from the pipelines we used the HSM flux ( $f$ : `base_SdssShape_instFlux`), the centroids ( $\vec{\ell}$ : `spotgrid_x/y`), and the elliptical Gaussian adaptive moments ( $I_{xx}$ ,  $I_{xy}$ , and  $I_{yy}$ : `base_SdssShape_xx/xy/yy`) quantities.

## 2.6. Vibration Correction

After completion of Run 5 data taking, systematic effects caused by the vibration of the spot projector setup were identified in the collected images. When the XY stage used to position the projector decelerated to a stop after a dither, a vibration with a long settling time was induced. As a result, the FWHM of the spots was systematically increased. The effects were significant on a sub-percent level for the positions, sizes and shapes of the spots.

The effects were removed by the following procedure. We assumed that the measurement residuals, e.g., second moments of brightness  $\delta I_{ij}$ , are to be zero on average. The measurement residuals for  $k$ -th exposure were fitted with a plane  $a_k x + b_k y + c_k$  by varying  $a_k, b_k, c_k$  for each exposure so that we minimize the summed square of the difference between the measurement residual and the plane model. If the effect was constant across the exposure subtracting off  $c_k$  should be enough. However, the subtraction of a plane from each exposure was needed empirically. The source could be the combination of the effects of vibrations and the tilt of the projector with respect to the focal plane that are different in different dithered exposures. The operation was applied for the  $\delta\ell$ ,  $\delta I_{ij}$ , and  $\delta f$  quantities exposure-by-exposure. In particular, this calibration had to be done in the second moments of brightness rather than the final products, such as ellipticities and shear, because they are not linear quantities under this operation.

## 3. DISTORTIONS OF PHOTOMETRY, CENTROID, PSF SIZE AND SHAPE

In this section, we report our measurements of the intrinsic sensor distortion in photometry, centroid, and PSF shape and size for six LSSTCam sensors. Then we describe the most important distortions revealed by the residual maps of the two CCD designs, ITL and e2v. The physical nature of the effects is discussed in Sections 5, 6.

### 3.1. *Effects of Sensor Anomalies on measurements*

We show the intrinsic sensor pixel response distortion maps in [Figure 3](#), which were created using calibrated flux, centroid, PSF size, and shape deviations measurements to reveal sensor anomalies as described in [Sec. 2.5](#).

We used a large collection of star-like exposures to obtain highly precise measurements. The faint sources were masked by selecting only the top 80%-th percentile of flux (see [Figure 1](#)). In addition, we binned the deviation measurements by pixel location and used super-pixels of size  $10 \times 10$  pixels to create the deviation maps, which were then stretched back to their original size.

For instance, in Run 5, which consisted of 2000 exposures, we achieved an RMS error on the astrometric shift maps of  $10^{-4}$  pixel (physical size = 1 nm), and  $10^{-5}$  on PSF-size/shape maps. Each exposure contained up to 2401 sources, resulting in an average of 10 sources per super-pixel.

The deviation maps for an E2V and an ITL sensor are presented in [Figure 3](#), with six different measurements shown for each sensor. Additional deviation maps for other sensors can be found in [Appendix B](#). To relate to the electric fields in the serial and parallel transfer directions of a sensor, we present the deviation maps separately for the  $x$  and  $y$  components. A brief description of each deviation map is provided.

**Photometry deviations:** This map corresponds to a “star flat” image but is made by stitching the deviations of flux measurements from the calibrated artificial stars. The e2v and ITL sensors display two distinct features in the maps: a rectangular shape associated with the 16 CCD segments, and irregular patterns resembling “coffee stains” in the ITL sensors and an “annealing pattern”, the diagonal stripes, in the e2v CCDs. The irregular patterns are created by the surface finish in the silicon manufacturing process. In particular the e2v sensor exhibits a radial gradient from the center to the corner, and bright corners are also observed in the ITL sensor. These features are likely to be a large-scale residual pattern from our spot-projector dithers. Some amplifiers have different contrasts showing distinct mean flux levels. These amplifier variations are due to the uncertainties on the gain estimation. These features are discussed further in [Sec. 6.1](#). The deviations presented here can be corrected in the on-sky survey by a flat-field correction because they are quantum efficiency variations, not pixel-area distortions.

**PSF size deviations:** The maps on the lower left in each group present the measured variations in the size of the PSF. The variations are at the sub-percent ( $\times 10^{-3}$ ) level. They are related to effects that increase or decrease the size of a point source. We do see a circular

ripple pattern centered on the outside of the sensor. We discuss this effect in [Figure 3](#). An unexpected structured variation in PSF size is also observed on the ITL sensors, with circles in three corners and a square in the middle. This pattern matches the hardware CCD frame that holds the detector. We investigate this feature further in [Sec. 6.4](#). It is important to note we do not see effects associated with the annealing pattern for the e2v sensor or associated with the coffee stain feature for the ITL sensor, which implies these features are not pixel-area distortions.

**Centroid deviations:** The two maps in the middle column show the  $x$  and  $y$  centroid deviations. The measurement displacement from the calibrated source is of order 0.01 pixel = 100 nm = 2 mas on the LSST focal plane. The circular pattern of the tree-ring effect is the most noticeable feature in the centroid residual maps. We analyze this effect further in [Sec. 5](#). In the ITL sensors, we do not see features related to the CCD shapes other than the mid-line break on the  $\delta y$  map. In contrast, a strong mid-line signal is evident for e2v along with strong contrast between the CCD segments’ edges in both directions ( $x$  and  $y$ ). Beyond those effects, we see irregular spatial feature variations in both CCDs.

**PSF shape deviations:** The two maps in the right-hand column show measured ellipticity variations from the calibrated spots. In R32-S01, three features are induced by 1) tree rings, 2) something else that causes a global variation, and 3) noisy regions where the population of spots is insufficient. General trends that  $e_1$  traces the tree-rings component along the axes ( $X$  and  $Y$ ) and  $e_2$  traces the component along the diagonal component  $X = Y$  (i.e.,  $45^\circ$ ) are apparent; see the explanation in [Sec. 5.2](#). The global variation and the noisy region make trends less striking, especially at the CCD edges where the number of stacked artificial stars is lower.

A summary and a comparison of the size of these effects are presented in [Table 1](#). The values in the table are the maximum absolute deviation values measured in the six CCDs examined in this study. Despite the small numbers, these features should meet the very restrictive requirements set by the LSST science goals (summarized briefly in the table). Complete descriptions may be found in the LSST Science Requirements Document ([Ivezic, and The LSST Science Collaboration 2011](#)), the LSST Science Book ([LSST Science Collaboration et al. 2009](#)) and ([The LSST Dark Energy Science Collaboration et al. 2018a](#), hereafter DESC2018).:

- psf-shape: uncertainties in the final LSST galaxy shear catalog are to be dominated by the statistical error ( $\sim \delta e$ ),  $10^{-3}$  (dimensionless), which sets

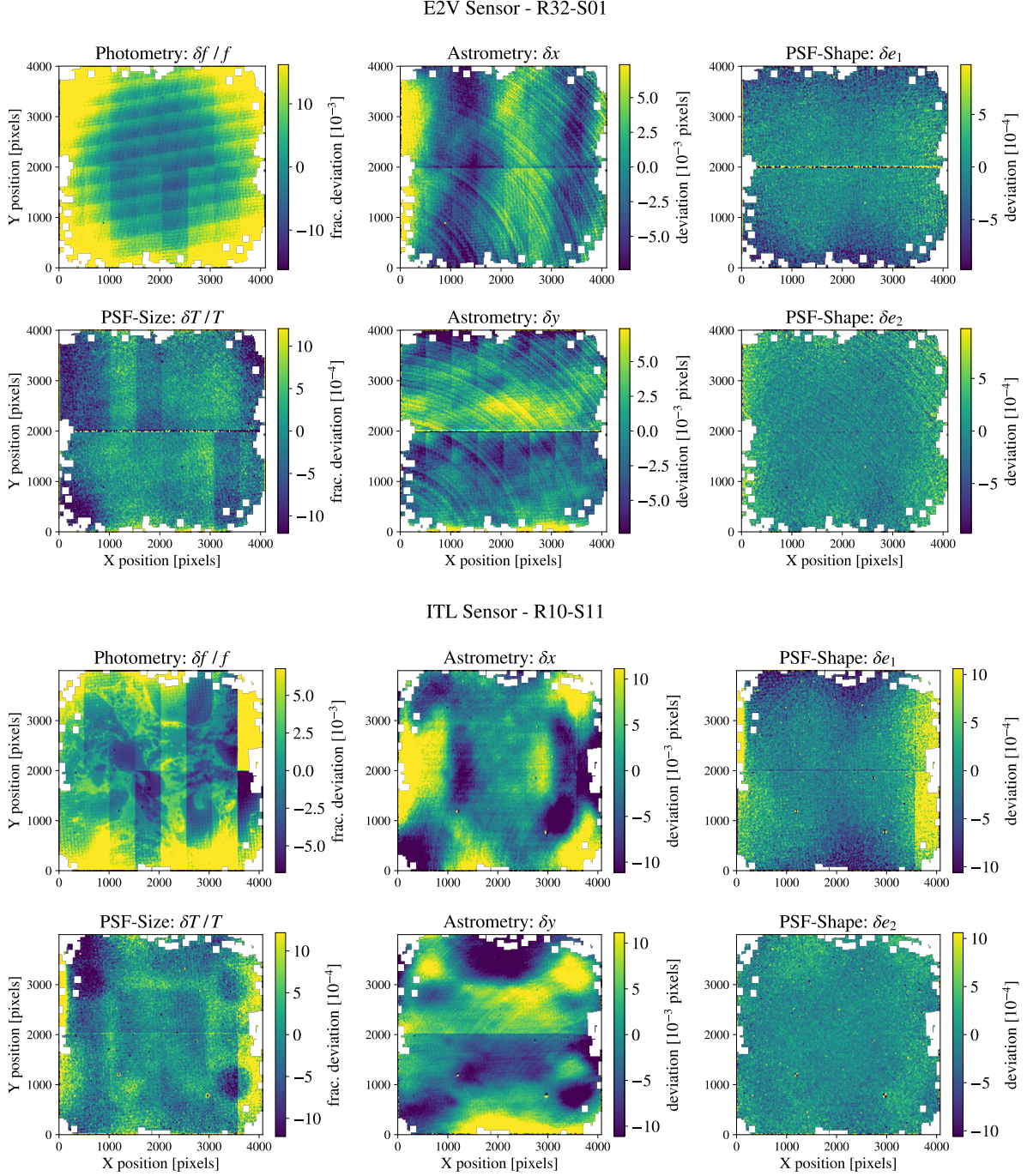


**Figure 3.** Maps of deviations of measurement quantities for two LSSTCam sensors, top: E2V R32-S01 and bottom: ITL R10-S11. The measured quantities are flux, PSF size, centroid, and shape. Shifts of centroid and shape shown in  $x$  and  $y$  components separately. The photometric map corresponds to a flat image for the sensor but made by stitching measurements of spots. Quantum efficiency variations across amplifiers are evident features in these maps. The structures in the PSF size, position, and shape residual maps are caused by pixel-area variation effects. Some striking examples are the tree-ring pattern and the amplifier boundary effects.

an upper limit on contributions from systematic errors (DESC2018).

- psf-size: the maximum acceptable PSF size bias  $\delta T/T$  is  $10^{-3}$  for the ten-year Rubin/LSST survey (DESC2018).



**Table 1.** Summary of the LSSTCam sensor effects limits on photometry (phot), centroid (center) and PSF-size and shape.

Origin	Name	Level				CCD Type
		phot. res [mmag]	centr. res [pixel]	psf-size frac. dev	psf-shape dev	
Scientific Goal	Requirements	< 10.0	< $5 \times 10^{-2}$	< $1 \times 10^{-3}$	< $1 \times 10^{-3}$	Both
	References	(a,b)	(a,b)	(c)	(a,c)	
Pixel-Area Variations	Mid-Line Break	–	< $4 \times 10^{-2}$	–	< $4 \times 10^{-3}$	Both
	Hardware Imprints	–	< $1 \times 10^{-2}$	< $1 \times 10^{-3}$	–	Both
	Amplifier Boundaries	–	< $4 \times 10^{-3}$	–	< $4 \times 10^{-4}$	Both
	Tree-Rings	–	< $4 \times 10^{-3}$	< $5 \times 10^{-4}$	< $5 \times 10^{-4}$	Both
Photometric Response	Radial Gradient	< 25.0	–	–	–	E2V
	Residual Impurities	< 4.0	–	–	–	Both
	Amplifiers Gain variation	< 1.0	–	–	–	Both

references: (a)LSST Science Collaboration et al. (2009); (b)Ivezić et al. (2019); (c) The LSST Dark Energy Science Collaboration et al. (2018b)

- photometric uncertainty: is expected to be below 10 mmag (Ivezić et al. 2019).
- astrometric uncertainty: for a single image is expected to be 10 mas (0.05 pixel) in order to achieve proper motion accuracy of 0.2 mas/yr and parallax accuracy of 1.0 mas for the 10 year survey (Ivezić, and The LSST Science Collaboration 2011).

The LSST requirements have been met with no corrections applied. Our findings show the small amplitude of the sensor QE, amplifier boundary, mid-line break and tree-rings distortions, and highlight the quality of the LSSTCam sensors. While these effects are small and the requirements are met, the effects are non-zero and can be mitigated with corrections at the image analysis stage. In the following sections, we will analyze these features comprehensively, present our physical interpretations, and discuss their impact on the LSST survey.

#### 4. EFFECTS OF EDGES, AMPLIFIER BOUNDARIES AND MID-LINE BREAK

This section closely examines the anomalies at the CCD sensors amplifier segments and edges.

The deviation maps have global features that can mask effects at the edges, amplifier boundaries, and the mid-line break. We remove such features by applying a high pass filter to the maps of variations with pixel periods higher than 250 pixels. Figure 4 presents the cleaned residual map of the e2v R32-S01 sensor on the left. We compute the signal profile in the  $x$  and  $y$  directions for bands of 500 pixels width as indicated in the left-hand plot. The middle and the right-hand columns show the resulting vertical and the horizontal signal profiles, respectively. In the signal profile plots, the amplifier boundaries and the mid-line break are represented

by grey dashed lines. We define the signal noise (red dashed lines) as the standard deviation of the signal.

The e2v sensor exhibits significant distortions in the vertical profiles, particularly at the mid-line break; we masked the mid-line break for visualization purpose. This feature is evident in all residual maps Figure 3, the peak is about 100 times greater than the noise for the y-component maps. Away from the mid-line, we see other patterns in the flux profile, for instance, the residual surface patterns (annealing and coffee stains) and increased distortion at the edges. The surface features for e2v and ITL sensors are QE deviations since they are not found in centroid or PSF measurements.

The mid-line break region has the only distortions that surpasses the LSST survey requirements (LSST Science Collaboration et al. 2009). The effect on the PSF measurements could be statistically significant; in such case, corrections are needed. The simplest approach is to mask the region as we did in Figure 4, albeit at the cost of losing approximately  $\Delta y = 20$  rows which corresponds to 0.5% of the sensor area. An alternative solution is to flag the sources detected within these areas as lower quality. An elaborate approach would be to model the distortion signal with a functional form, under the assumption that the effect is static. This approach is somewhat similar to the brighter-fatter effect correction in that regard (e.g., Lage et al. 2017). Further assessment of the feasibility of such corrections is needed. For the amplifier boundaries, similar solutions as for the mid-line break could be implemented.

#### 5. TREE-RINGS

In this section we focus on the signatures of tree-rings. We first present the relation between the flat-field distortion due to tree rings and centroid and PSF shape and size changes. Then, we describe our method to measure



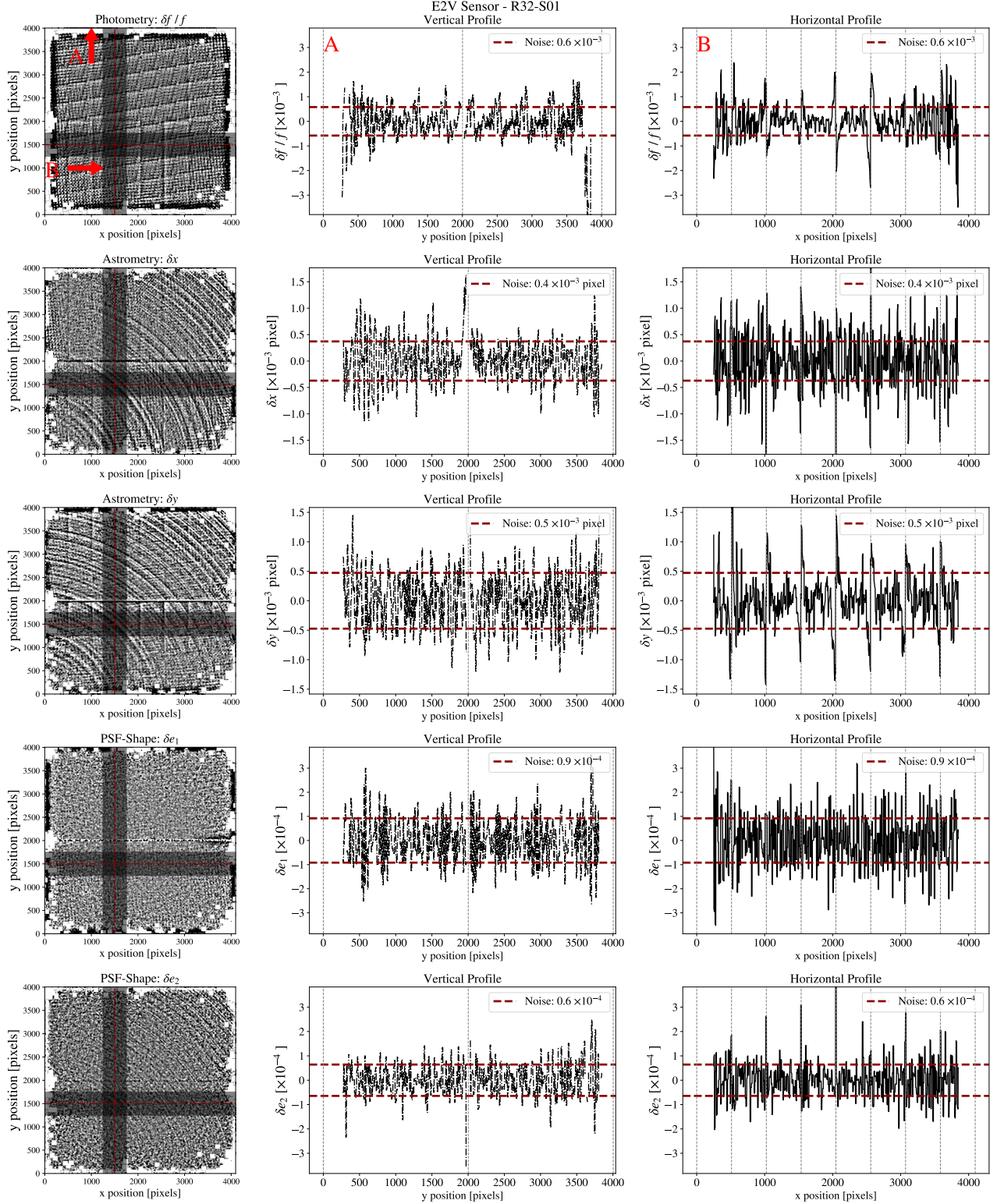


**Figure 4.** Distortion maps (left) and signal distortion profile across the horizontal (middle) and vertical (right) directions. A high-pass filter was applied to the images in the left-hand column to highlight the high-frequency distortions. The profiles are the map signal computed over the regions of the gray bands; the red dashed lines indicate the error level (rms). In the right, the  $e_1$  and  $\delta x$  horizontal profiles show the effects at the amplifier boundaries (gray dashed lines). In the middle column, the mid-line break is the most noticeable feature, especially for  $\delta y$ , with a signal level  $100\times$  higher than the noise.

the tangentially averaged effects in the polar coordinate system. Finally, we present the tree-rings oscillatory radial distortions and compare them with the flat-field signal.

### 5.1. Pixel Area Variation

In [Plazas et al. \(2014a,b\)](#), the tree-ring effect in the DECam camera sensors is interpreted as effective changes of pixel area caused by a lateral electric field. Any quantities dependent on the pixel area are affected by this distortion. Here we follow the same approach to interpret the tree-ring effect in the LSST sensors in terms of pixel area changes.

The centroid shifts are modeled as the displacement  $d(r)$  of the centroid of photons incident at a radial distance  $r$  from the inferred center of the tree-rings compared to the actual radial displacement from the center  $r_0 = r - d(r)$ . Then, the corresponding area distortion,  $w(r)$ , can be calculated as the Jacobian determinant of the coordinate transformation  $r \rightarrow r_0$  ([Plazas et al. 2014a,b](#); [Okura et al. 2015](#)):

$$1 + w(r) = \left| \frac{r_0 dr_0 d\theta}{r dr d\theta} \right| \approx \left| \frac{(r - d(r))(dr - \partial_r d(r) dr)}{r dr} \right|, \quad (13)$$

At the first order one can show:

$$w(r) = -\frac{\partial d(r)}{\partial r} - \frac{d(r)}{r} \approx -\frac{\partial d(r)}{\partial r}. \quad (14)$$

The second term is negligible for  $r > 10^3$  pixels where the LSST tree-rings signal is nonzero, given that  $d(r)$  is on the order of ten times larger than  $\partial_r d(r)$ . Note that we follow the definition of [Okura et al. \(2015\)](#) for the distortion of  $d(r)$ . As a result, equation [Equation 14](#) has sign opposite to the convention in [Plazas et al. \(2014a\)](#).

Further, we can define magnification in size  $T^{1/2}$  and change in ellipticity  $\delta e$  and relate them to the area perturbation  $w(r)$ . The perturbation on  $T^{1/2}$  can be written as ([Okura et al. 2015](#)):

$$\frac{(T + \delta T)^{1/2} - T^{1/2}}{T^{1/2}} = -\frac{1}{2} \left( \frac{\partial d(r)}{\partial r} + \frac{d(r)}{r} \right) = -\frac{1}{2} w(r). \quad (15)$$

For a first order expansion,

$$\frac{(T + \delta T)^{1/2} - T^{1/2}}{T^{1/2}} \approx \frac{\delta T}{2T}. \quad (16)$$

Thus, the fractional change in PSF size is equal to the opposite of the flat-field distortion:

$$\frac{\delta T}{T} = -w(r), \quad (17)$$

Similarly, the change in shear due to the tree-rings  $\gamma_{TR}$  ([Okura et al. 2015](#)) in conjunction with equation [14](#) can be shown to be:

$$\begin{aligned} \gamma_{TR}(r) &= \frac{1}{2} \left( \frac{\partial d(r)}{\partial r} - \frac{d(r)}{r} \right) = -\frac{1}{2} \left( w(r) - 2\frac{d(r)}{r} \right) \\ &\approx -\frac{1}{2} w(r). \end{aligned} \quad (18)$$

Our ellipticity definition, [Equation 7](#), is a factor 2 times the shear ([Schneider 2005](#)); thus we can write:

$$\delta e_r \approx 2\gamma_{TR} \approx -w(r). \quad (19)$$

Equations [17](#), [19](#) equate the PSF size and shape distortions to the opposite of the flat-field distortion  $w(r)$ .

### 5.2. Tree-Rings Coordinate System

The centroid and shape tree-rings distortions depend on the coordinate system. In contrast, the PSF-size and the flat-field distortions are invariant under a change of coordinate system. To measure the tree-ring distortion effects, we transform  $(\ell_x, \ell_y)$  and  $(e_1, e_2)$  to polar coordinates by applying the rotation matrix. The main difference between centroid and shape is the rotation matrix. Ellipticities are pseudo-vectors, thus, their transformation is:

$$\begin{pmatrix} e_r \\ e_\theta \end{pmatrix} = \begin{pmatrix} \cos 2\phi & \sin 2\phi \\ \sin 2\phi & -\cos 2\phi \end{pmatrix} \begin{pmatrix} e_1 \\ e_2 \end{pmatrix}, \quad (20)$$

where  $\phi = \tan^{-1} \left( \frac{y-y_0}{x-x_0} \right)$ . The center of this coordinate system  $(x_0, y_0)$  is the center of the tree-rings circles, which is outside the CCD. The factor  $2\phi$  is a consequence of the invariance of ellipticities against  $180^\circ$  rotations. For this reason, the tree-rings signal in the  $e_1$  component is always less than for the  $e_2$  component at the CCD diagonal  $X = Y$  (i.e.,  $45^\circ$ ), since the  $\cos(2\phi)$  term is zero for  $\phi \approx 45^\circ$  or  $135^\circ$ . One can visually confirm that the tree-rings signal vanishes at the diagonal in the  $e_1$  PSF-shape maps (see [Figure 3](#)). In contrast, this signal is higher along the  $X$  and  $Y$  axes as you can see in the maps with large tree-rings amplitude, e.g. R24-S11 and R02-S02 ([Figures 7, 8](#)). However, for the sensors with low tree-ring amplitudes the noise at the CCD edges hides the rings features.

### 5.3. Algorithm

As we saw in the previous sections, our residual maps have the tree-rings and other features, such as global variations or structures associated with the amplifier boundaries. Therefore, to determine the components due to tree-rings, we perform image processing described in the following steps:

1. Image pre-processing: We clean the residual images. As other effects impact the residual maps at larger angular scales, we apply a high-pass filter to highlight the tree-ring effects. First, we binned the maps by  $8 \times 8$  pixels to increase the signal-to-noise ratio of the features and apply a high-pass filter to remove the global variation with pixel frequency higher than 250 pixel, as described in Park et al. (2020). During this process, we also identify bad pixels and mask them. Finally, the image is stretched to the original size.
2. Polar Transformation: We convert the original rectangular CCD pixel image  $(x,y)$  to the polar coordinate system with respect to the tree-rings center. We use (`warpPolar` from `OPENCV`) and the wafer center (Park et al. 2020). In this operation, the output is an image in  $(r, \theta)$  coordinates where  $r$  is the distance from the tree-rings center. In this step, we check whether the steps above are successful by examining the transformed image. If the tree-rings center is misidentified, the straight line of the tree-rings along with the  $\theta$  direction would be tilted or disturbed.
3. Extracting the profile: We average the  $(r, \theta)$  image over  $\theta$  to evaluate the profile in  $r$ .

The tree-rings center can be approximated by the center of the silicon wafer in most cases (see their figure 2. Park et al. 2017). However, we noticed a center mismatch in some cases after visually inspecting the polar images. Since these mismatches affected the tree-rings signal, we measured the tree-rings center on flat-field images with a back-bias voltage equal to zero, as the signal is more prominent at this voltage setup (Park et al. 2017). Following Park et al. (2017, 2020) algorithm, we fit tree-rings center values using 30 flat-field images. This verification test showed that the differences between the silicon wafer center and the actual center have an r.m.s of 75 pixel. For the cases where the signal was affected by the center mismatch we use the fitted values.

#### 5.4. Measured Distortions Due to Tree Rings

Using the procedure described in Sec. 5.3, we extracted the one-dimensional profiles of distortions due to tree-rings, finding amplitudes at the  $10^{-4}$  level for centroid, PSF shape, and size distortions.

Figure 5 shows the radial profiles of the oscillating distortions. For the centroid shift, we show the derivative of the centroid shift with respect to the radius. In this case, we used a `savgol_filter` with a window size of

the typical tree-rings frequency, 72 pixels (Park et al. 2020).

As described in the Sec. 5.1, the tree-rings distortions of centroid and PSF shape and size are directly related to the distortions inferred from flat-field images; see, e.g., Equation 19. For this reason, on each plot we overlay the distortions inferred from flats. Although measured distinctly, the distortions that we infer from tree-ring effects are very close to the direct measurement of the flat-field image distortions presented in Sec. 3. The amplitudes and the phases of the oscillations matches qualitatively the flat-field signal.

To confirm the pixel-area distortions relations (Sec. 5.1), we fit the normalization factor from equations 14, 17, 19. The fitted relation results are presented in the lower left corner of each panel in Figure 5. Overall, the fitted parameters are close to unity, validating the tree-ring effects impact on pixel-area quantities. The error of the fit indicated by the RMS error is on the order of  $(5 - 10) \times 10^{-5}$ , which is about the same noise we measured in the vertical and horizontal profile for PSF-shape (Figure 4).

#### 5.5. Corrections: Tree-Rings

The centroid displacements due to tree-ring effects are smaller than needed to satisfy the LSST science requirements on centroid (The LSST Dark Energy Science Collaboration et al. 2018b). Nevertheless, given the exquisite control on systematics demanded by LSST, the tree-ring effects could be corrected by measuring their radial profiles from flats (and photometry) and star flats (centroid; or using the formula 14 to extract the profiles of centroid shifts from flats). The profiles would be incorporated as templates in the centroid and photometric solution optimization during image reduction, with an amplitude parameter that depends on the filter band (e.g.: Plazas et al. 2014a,b; Bernstein et al. 2017a, 2018, 2017b)).

The approach of Bernstein et al. (2017a) could be incorporated into the pipelines (Bosch et al. 2018, 2019) for correcting centroid distortions. Although the DECam detectors show PSF size distortions similar to the tree-rings even after applying their methodology (Jarvis et al. 2021), we believe that would not be the case here. For DECam, the remaining PSF size distortions are likely due to charge diffusion. The LSSTCam PSF-size distortions follow a one-to-one relation with the flat-field signal (see Figure 5), indicating that the main contributions are predominantly pixel-area distortions as demonstrated in Sec. 5.1.

## 6. OTHER EFFECTS

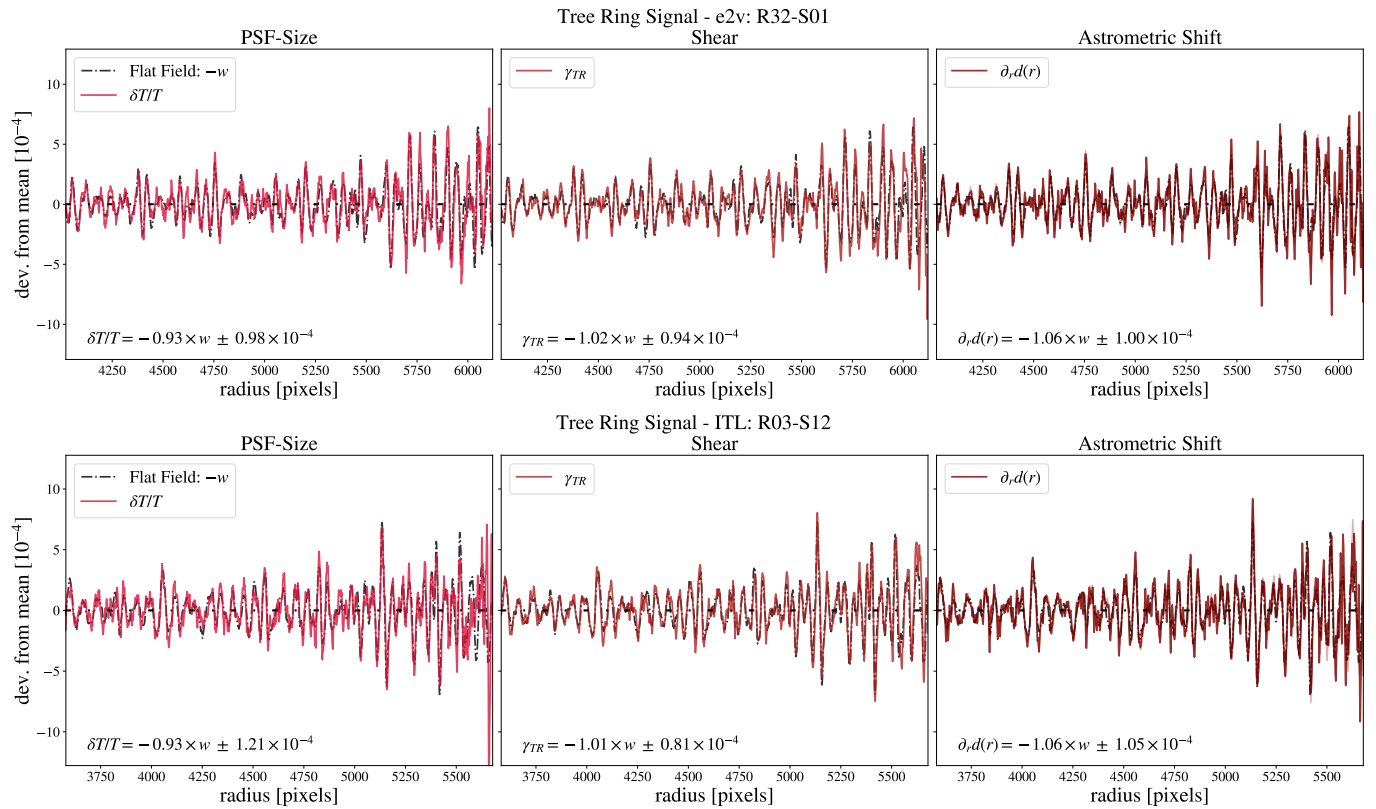


**Figure 5.** Distortions due to tree-rings for PSF size (left), shape (middle) and centroid (right) deviations as a function of distance from the tree rings center for the sensors R32-S01 (top) and R03-S12 (bottom). The flat field distortion  $w(r)$  (black dashed line) signal is correlated with the tree-rings signal (colored solid lines). In the lower-left corner of each panel, the fitted linear relation between the two signals is displayed alongside the RMS error of the fit. The slope is close to unity, confirming the tree-rings effect. To highlight the oscillatory features of the signal, the radius range was limited to 2100 pixels up to the maximum radius. Note that the centroid shift is related to the derivative of the tree-rings distortions.

In addition to the tree-ring effects, we discuss a couple of other effects that we observed in Sec. 4.

### 6.1. Quantum Efficiency Variations

The patterns in the photometric residual maps for e2v and ITL are different. The detailed patterns can be interpreted as quantum efficiency variations that are caused by the back-side surface finish in the manufacturing process. The ITL pattern in the flux distortion map (coffee stains) is due to a layer of non-stoichiometric oxidized silicon and cleaning residue of acid on the silicon surface right after etching, creating some non-uniformity in backside charging (Bajat et al. 2020). Instead, the e2v sensors have a regular striped pattern in the flux distortion map which appears to be caused by the laser annealing process after the thinning process in the CCD fabrication (Burke et al. 2004; Radeka 2006; Bender et al. 2014). This residual surface effect is generally greater at shorter wavelengths since the blue photons are converted close to the CCD back-side. The amplitude of this effect should be at most  $10^{-2}$  and almost undetectable in redder wavelengths than  $\sim 500$  nm from the verifica-

tion tests on flat-fields (Park et al. 2017; Roodman et al. 2018).

The origin of the radially symmetric gradients in e2v maps is not clear. We do not see a similar pattern in regular flat images taken with a flat illuminator. The dithering of the spot projector might cause this pattern; however, the fact that the maps for ITL based on the same projector dithering pattern do not have the same radially symmetric pattern suggests otherwise. Further investigation using on-sky images will give more understanding of this effect.

### 6.2. Gain Mis-Matches Between Segments

The Figure 3 shows different mean flux values across the different segments within  $10^{-3}$  variation. These differences can be a result of the gain ( $e^-/\text{ADU}$ ) measurement uncertainty. The accuracy of our gain determination was of the order  $10^{-3}$ , which is comparable to the level of the discontinuity. To mitigate the discontinuity, an adjustment using the imaging region could be used. However, this is outside the scope of this paper.



In addition, there are extreme examples, for instance the R03-S12 sensor, for which the amplifier at the bottom right shows a percent-level gain contrast. This segment was affected by stray light reflections from the side of the cryostat window. As a result, the shadow made a significant impact on the gain determination.

### 6.3. Mid-line Break & Amplifier Boundaries

The mid-line break, which divides the top and bottom halves of the CCDs, is the most striking sensor feature, clearly visible in the map of both types of sensor [Figure 3](#). Also evident are features associated with the readout amplifier boundaries, which divide the sensors vertically. These effects are stronger for the e2v CCDs and can be up to  $\times 10$  greater than for ITL sensors. This difference stems from design differences for the electronic readouts. For instance, e2v CCDs have a physical boundary that blocks electron flow between the upper and lower halves. On the other hand, ITL sensors have less-prominent mid-line effects because they have channel stops in the electronics readout similar to the amplifier boundary structures. The importance of the mid-line can vary between the sensors of the same design and can be greater than reported here.

Another important spatial distortion reported for LSSTCam CCDs is edge effects ([Bradshaw et al. 2018](#)). The metallization around the edges of the CCDs is set at a positive potential that induces a lateral electric field shift extending up to  $\geq 10$  pixels into the bulk. The footprint of the artificial stars is not extended enough to cover the CCD edges, so we cannot provide any guidelines about edge effects from this work. However, CCD edge effects also should be taken into account in image reduction.

### 6.4. Imprints From Hardware Structure: CCD Frame

Multiple effects leave their imprints on the centroid and PSF-size maps of several sensors, including ITL’s R03/S12, R10/S11, and e2v’s R22/S11. In [Figure 6](#), the PSF size map of R10/S11 is shown alongside a photo of the ITL CCD support structure. Interestingly, the structure in the residual maps aligns with the location of the alignment pins and the hold-downs ([Lesser & Ouellette 2017](#)).

For the DECam CCDs, [Bernstein et al. \(2017a, see Figure 8\)](#) showed that the connectors impact their astrometry (centroid) when stacking all CCD images with different wavelengths (in the *gri* bands). They concluded this is likely results from stresses induced in the CCD lattice by the connector or the hole in the mounting board. In addition, they also identified a wavelength-dependent feature related to the CCD frame

metallic structure ([Bernstein et al. 2018](#)). The effect was strongest for the Y filter owing to the reflectivity of the metal structure, because a significant fraction of the infrared photons pass through the sensor. However, the ITL sensors for LSST have a highly IR-absorbing material “lithoblack” deposited on the sensor wafer’s front side surface to prevent such an effect ([Lesser & Ouellette 2017](#)). In any case reflection of blue photons that would have passed through the CCD is implausible.

This effect might potentially impact the survey, as affected regions are close to the 0.1% threshold limit set by LSST requirements. For instance, other focal plane sensors not probed in this work may have greater distortions, which could leave imprints in astrometry and PSF-size data at the focal plane level. In contrast, [Bernstein et al. \(2018\)](#) chose to leave the affected regions uncorrected since they were not found to be associated with significant effects. Further assessment of this systematic error on the LSSTCam focal plane CCDs should be performed.

### 6.5. Artifacts

The photometry distortion map of the sensor R22-S11 ([Figure 8](#); see top panel) has a noisy pattern. We do not have a clear explanation for this effect. It is likely caused by code failures related to determining the flux normalization since the other maps do not have corresponding effect.

Features caused by a fingerprint on the aperture window of the test apparatus were apparent in few residual maps. The sensor ITL R02-S02 ([Figure 8](#)) has a visible shadow feature (roughly square) in photometry distortion maps at  $x \approx 2500, y \approx 1500$ . A similar but less striking pattern appears in the astrometry and PSF size and shape measurements. For the ITL R03-S12 sensor ([Figure 3](#)), a less striking feature can be seen at  $x = 2500, y = 1500$  in the PSF shape and astrometry maps.

## 7. DISCUSSION

### 7.1. Limitations

This work represents a pilot study to probe the impact of LSSTCam sensor effects on the LSST survey. Although the findings and the data presented here are quantitative, they are for only a small subset of the LSSTCam CCDs and are not intended to be used for LSSTCam calibrations. The dataset for calibrations will be built during the first months of Rubin observatory operations. Star flats should be created for the complete sets of sensors and filters.

Potential limitations of this study should be kept in mind. The pre-processing described in [Section 2.6](#) could

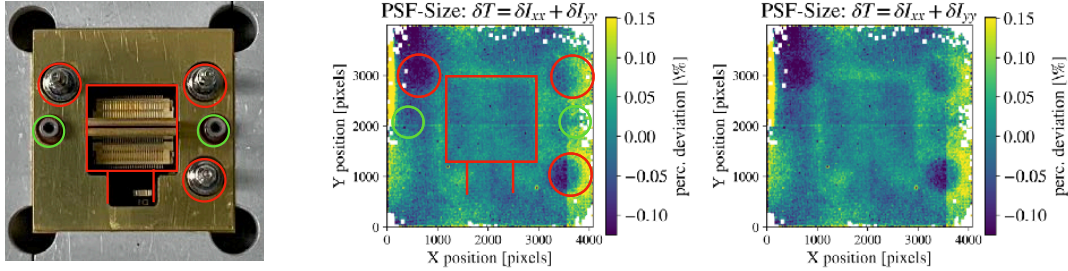


**Figure 6.** Left: The back structure of the ITL CCD (gold) is seen with two alignment pins (green) and three hold-downs (red). The connector to the flex cable is within the center box, where no gold metal support is present. Middle and right: PSF size residual map without and with a CCD frame drawing (red). The distortions of PSF size follow the shape of the CCD support frame.

potentially remove linearly varying features, or add any sensor systematics of larger size than the extent of the spots. To mitigate these considerations, we introduced a dithered pattern for the spot projector grid and calculated the average values of measurements by averaging all 2000 dithered images spanning the CCD, shown in Figure 2. The detailed features such as the annealing pattern, coffee stain, tree-rings are real, but global variations could potentially be artifacts of this pre-processing. On-sky testing will answer the question.

Also, our study is limited to just a single wavelength range, around 450 nm. For the LSST survey the wavelength dependence of sensor anomalies should be evaluated, particularly their effects on PSF size and shape (Meyers & Burchat 2015; Kamath et al. 2020). Also, fringing effects in the y-band should be quantified and the proposed corrections for fringing validated (Guo et al. 2022).

Finally, our study focused only on selected sensors. The sensor anomalies over the full focal plane as well as all other wavelengths will be investigated when the observatory collects on-sky data.

### 7.2. Tearing mitigation

We observed tearing along the mid-line break in the Run 3 period. This effect can be explained by the electric field distortions created at the boundaries between channels, caused by the non-uniform distribution of holes around the channel stop (Juramy et al. 2020, see their Section 2.2.3). The cause of the tearing effect has been attributed to the CCD readout procedure, in particular, the parallel clocking operation. Juramy et al. (2020) suggested mitigations via changing the readout voltage setup. Between Runs 3 and 5, significant efforts were implemented to mitigate this feature, including changing the readout voltages (see Table 2)

This change in operation voltage made a significant impact on the tearing features, mostly invisible to the eye. However, we did not find any obvious improvement

or decrease of the effects at the amplifier boundaries and at the mid-line break. When we compare two set of profiles of R32-S01 (Run5) or R24-S11 (Run 5) and R22-S11 (Run 3) in the Appendix, the mid-line break and amplifier boundaries distortion are approximately the same.

### 7.3. Tree-Rings In Other CCD Devices

The presence of tree-ring features is reported in other large CCDs cameras such as DECam (Flaugher et al. 2015b), Hyper Suprime-Cam (Kamata et al. 2014a), and PanSTARRS GPC1 (Magnier et al. 2018). The relative amplitudes of the effect range from 0.1% to 10% in those systems.

Plazas et al. (2014b) reported the amplitude of tree-ring effects in DECam flat images is at the 1–10% level and concluded their nature is pixel size variations by comparing their photometric and centroid deviations. A similar effect has also been reported in the Hyper Suprime-Cam (Kamata et al. 2014b).

In contrast, a unique effect, referred to as ‘charge diffusion’, was identified in the GPC1 detectors (Magnier et al. 2018). Although this effect displays similarities to the tree-ring signal in terms of photometry and PSF size, it is actually driven by variations in the rate of vertical charge transportation. The primary outcome is a charge diffusion of variable length that predominantly affects the PSF size, but not the shape.

Later, the tree-rings effect on PSF-size was also seen in a few CCDs in DECam, after application of a correction for tree-ring distortion based on astrometric shifts (Jarvis et al. 2021). Their residual signal amplitude was much more prominent in the blue band, which indicates it occurs at the surface where light enters the CCD. Their could be interpreted as being due to charge diffusion.

In this study, we compared  $(dT/T)$ , shape  $\delta e$ , and centroid shift  $d(r)$  distortions and the flat signal  $w(r)$ . We fitted a linear relation between these signals and found

near direct proportionality as predicted by equations 14, 17, 19. Consistent with the findings of (Plazas et al. 2014b), we interpret the effects caused by tree-rings as being due to shifts in parallel electric fields. Although charge diffusion variability effects can be present in the LSSTCam sensors the correlations between  $dT/T$  and  $w(r)$  did not significantly depart from unity. Studies at redder wavelengths could potentially show different characteristics of the tree-rings signals on PSF-size due to diffusion effects.

## 8. CONCLUSION

This work represents the first probe of the impact of CCD anomalies on photometry, centroid and PSF measurements of the LSSTCam. We analyze the impacts using measurements artificial stars on a subsample of six LSSTCam sensors. We classify a variety of distortions according to their source: CCD mid-line break, hardware imprints, amplifier boundaries and tree-rings. We report our main findings below.

- The centroid distortions are lower than the requirements on astrometric systematic errors of a single image (Ivezić et al. 2019). The largest centroid distortions are due to the mid-line break, a design feature present only on the e2v sensors in LSSTCam. The ITL sensors have an unexpected hardware imprint from the metallic structure of the CCD frame and the effect is not large than the mid-line. The centroid distortions due to amplifier boundaries and tree-rings, are  $10\times$  smaller effects.
- The shape distortions presented here are similar to the centroid ones. However, the amplitude of the mid-line break distortion in the shape measurements is slightly greater than the LSST requirement. Since the area affected is less than 0.5% of the CCD area we suggest masking a region around the mid-line of e2v CCDs during image reduction.
- The photometric distortions originate with spatial variation of quantum efficiency; their effect is

not higher than 3 mmag. The main features observed are due to gain variations between the sixteen CCD segments and global pattern features. The global features distortions have distinct visual appearance between the two CCD designs. For ITL sensors, the distortions have the appearance of ‘coffee stains’ while for e2v sensors the appearance is due to laser annealing. The differences may be traced to differences in the manufacturing processes, in particular, the CCD back-side silicon treatment procedure.

- The tree-rings distortion effect measured for centroid shift is of the order of  $10^{-4}$  pixel and  $10^{-5}$  for PSF size and shape. These changes can be related to the distortions measured in flat-fields through the transformation defined in equations 14, 17, 19. Therefore, if necessary the effect can be corrected with the use of flat-field template signals.

We find variations in distortion even among sensors from the same vendor. Further on-sky studies are needed to probe the variation of these effects for the 189 LSSTCam science sensors, as well as to study their dependence on wavelength. The laboratory study we present here provides a foundation for understanding those effects in the entire focal plane using on-sky data.

## 9. ACKNOWLEDGMENTS

We sincerely thank the anonymous referee for their thorough review of this manuscript and their invaluable feedback. This material is based upon work supported in part by the National Science Foundation through Cooperative Agreement AST-1258333 and Cooperative Support Agreement AST-1202910 managed by the Association of Universities for Research in Astronomy (AURA), and the Department of Energy under Contract No. DE-AC02-76SF00515 with the SLAC National Accelerator Laboratory managed by Stanford University. Additional Rubin Observatory funding comes from private donations, grants to universities, and in-kind support from LSSTC Institutional Members.

## REFERENCES

- Arndt, K., Riot, V., Alagoz, E., et al. 2010, in Society of Photo-Optical Instrumentation Engineers (SPIE) Conference Series, Vol. 7736, Adaptive Optics Systems II, ed. B. L. Ellerbroek, M. Hart, N. Hubin, & P. L. Wizinowich, 773662, doi: [10.1117/12.857829](https://doi.org/10.1117/12.857829)
- Astier, P. 2015, Journal of Instrumentation, 10, C05013, doi: [10.1088/1748-0221/10/05/C05013](https://doi.org/10.1088/1748-0221/10/05/C05013)
- Bajat, A., Christov, A., Karpov, S., & Prouza, M. 2020, in Society of Photo-Optical Instrumentation Engineers (SPIE) Conference Series, Vol. 11454, Society of Photo-Optical Instrumentation Engineers (SPIE) Conference Series, 114542D, doi: [10.1117/12.2559946](https://doi.org/10.1117/12.2559946)

- Bender, D. A., DeRose, C. T., Starbuck, A., Verley, J. C., & Jenkins, M. W. 2014, in *Laser Applications in Microelectronic and Optoelectronic Manufacturing (LAMOM) XIX*, ed. Y. Nakata, X. Xu, S. Roth, & B. Neuenschwander, Vol. 8967, International Society for Optics and Photonics (SPIE), 89670S, doi: [10.1117/12.2037339](https://doi.org/10.1117/12.2037339)
- Bernstein, G. M., & Jarvis, M. 2002, *AJ*, 123, 583, doi: [10.1086/338085](https://doi.org/10.1086/338085)
- Bernstein, G. M., Armstrong, R., Plazas, A. A., et al. 2017a, *PASP*, 129, 074503, doi: [10.1088/1538-3873/aa6c55](https://doi.org/10.1088/1538-3873/aa6c55)
- Bernstein, G. M., Abbott, T. M. C., Desai, S., et al. 2017b, *PASP*, 129, 114502, doi: [10.1088/1538-3873/aa858e](https://doi.org/10.1088/1538-3873/aa858e)
- Bernstein, G. M., Abbott, T. M. C., Armstrong, R., et al. 2018, *PASP*, 130, 054501, doi: [10.1088/1538-3873/aaa753](https://doi.org/10.1088/1538-3873/aaa753)
- Bosch, J., Armstrong, R., Bickerton, S., et al. 2018, *PASJ*, 70, S5, doi: [10.1093/pasj/psx080](https://doi.org/10.1093/pasj/psx080)
- Bosch, J., AlSayyad, Y., Armstrong, R., et al. 2019, in *Astronomical Society of the Pacific Conference Series*, Vol. 523, *Astronomical Data Analysis Software and Systems XXVII*, ed. P. J. Teuben, M. W. Pound, B. A. Thomas, & E. M. Warner, 521, doi: [10.48550/arXiv.1812.03248](https://doi.org/10.48550/arXiv.1812.03248)
- Bradshaw, A. K., Lage, C., & Tyson, J. A. 2018, in *Society of Photo-Optical Instrumentation Engineers (SPIE) Conference Series*, Vol. 10709, *High Energy, Optical, and Infrared Detectors for Astronomy VIII*, ed. A. D. Holland & J. Beletic, 107091L, doi: [10.1117/12.2314276](https://doi.org/10.1117/12.2314276)
- Burke, B., Gregory, J., Loomis, A., et al. 2004, in *IEEE Nuclear Science Symposium*, Vol. 51, *IEEE Trans. On Nucl. Sci.*, doi: [10.1109/NSSMIC.2003.1352062](https://doi.org/10.1109/NSSMIC.2003.1352062)
- Doherty, P. E., Antilogus, P., Astier, P., et al. 2014, in *Society of Photo-Optical Instrumentation Engineers (SPIE) Conference Series*, Vol. 9154, *High Energy, Optical, and Infrared Detectors for Astronomy VI*, ed. A. D. Holland & J. Beletic, 915418, doi: [10.1117/12.2056733](https://doi.org/10.1117/12.2056733)
- Flaugher, B., Diehl, H. T., Honscheid, K., et al. 2015a, *AJ*, 150, 150, doi: [10.1088/0004-6256/150/5/150](https://doi.org/10.1088/0004-6256/150/5/150)
- . 2015b, *AJ*, 150, 150, doi: [10.1088/0004-6256/150/5/150](https://doi.org/10.1088/0004-6256/150/5/150)
- Gruen, D., Bernstein, G. M., Jarvis, M., et al. 2015, *Journal of Instrumentation*, 10, C05032, doi: [10.1088/1748-0221/10/05/C05032](https://doi.org/10.1088/1748-0221/10/05/C05032)
- Guo, Z., Walter, C. W., Lage, C., Lupton, R. H., & The LSST Dark Energy Science Collaboration. 2022, arXiv e-prints, arXiv:2211.09149, doi: [10.48550/arXiv.2211.09149](https://doi.org/10.48550/arXiv.2211.09149)
- Hirata, C., & Seljak, U. 2003, *MNRAS*, 343, 459, doi: [10.1046/j.1365-8711.2003.06683.x](https://doi.org/10.1046/j.1365-8711.2003.06683.x)
- Holland, S. E., Bebek, C. J., Kolbe, W. F., & Lee, J. S. 2014, *Journal of Instrumentation*, 9, C03057, doi: [10.1088/1748-0221/9/03/C03057](https://doi.org/10.1088/1748-0221/9/03/C03057)
- Holland, S. E., Groom, D. E., Palaio, N. P., Stover, R. J., & Wei, M. 2003, *IEEE Transactions on Electron Devices*, 50, 225, doi: [10.1109/TED.2002.806476](https://doi.org/10.1109/TED.2002.806476)
- Holland, S. E., Kolbe, W. F., & Bebek, C. J. 2009, *IEEE Transactions on Electron Devices*, 56, 2612, doi: [10.1109/TED.2009.2030631](https://doi.org/10.1109/TED.2009.2030631)
- Ivezić, Ž., Kahn, S. M., Tyson, J. A., et al. 2019, *ApJ*, 873, 111, doi: [10.3847/1538-4357/ab042c](https://doi.org/10.3847/1538-4357/ab042c)
- Ivezić, and The LSST Science Collaboration. 2011, *LSST Science Requirements Document*, Lsst document, LSST. <https://ls.st/LPM-17>
- Jarvis, M., Bernstein, G. M., Amon, A., et al. 2021, *MNRAS*, 501, 1282, doi: [10.1093/mnras/staa3679](https://doi.org/10.1093/mnras/staa3679)
- Juramy, C., Antilogus, P., Le Guillou, L., & Sepulveda, E. 2020, arXiv e-prints, arXiv:2002.09439. <https://arxiv.org/abs/2002.09439>
- Juramy, C., Antilogus, P., Bailly, P., et al. 2014, in *Society of Photo-Optical Instrumentation Engineers (SPIE) Conference Series*, Vol. 9154, *High Energy, Optical, and Infrared Detectors for Astronomy VI*, ed. A. D. Holland & J. Beletic, 91541P, doi: [10.1117/12.2055175](https://doi.org/10.1117/12.2055175)
- Kaiser, N., Squires, G., & Broadhurst, T. 1995, *ApJ*, 449, 460, doi: [10.1086/176071](https://doi.org/10.1086/176071)
- Kamata, Y., Nakaya, H., Kawanomoto, S., & Miyazaki, S. 2014a, in *Society of Photo-Optical Instrumentation Engineers (SPIE) Conference Series*, Vol. 9154, *High Energy, Optical, and Infrared Detectors for Astronomy VI*, ed. A. D. Holland & J. Beletic, 91541Z, doi: [10.1117/12.2055763](https://doi.org/10.1117/12.2055763)
- Kamata, Y., Nakaya, H., Kawanomoto, S., & Miyazaki, S. 2014b, in *Society of Photo-Optical Instrumentation Engineers (SPIE) Conference Series*, Vol. 9154, *High Energy, Optical, and Infrared Detectors for Astronomy VI*, ed. A. D. Holland & J. Beletic, 91541Z, doi: [10.1117/12.2055763](https://doi.org/10.1117/12.2055763)
- Kamath, S., Meyers, J. E., Burchat, P. R., & (LSST Dark Energy Science Collaboration. 2020, *ApJ*, 888, 23, doi: [10.3847/1538-4357/ab54cb](https://doi.org/10.3847/1538-4357/ab54cb)
- Kotov, I. V., Haupt, J., O'Connor, P., et al. 2016, in *Society of Photo-Optical Instrumentation Engineers (SPIE) Conference Series*, Vol. 9915, *High Energy, Optical, and Infrared Detectors for Astronomy VII*, ed. A. D. Holland & J. Beletic, 99150V, doi: [10.1117/12.2231925](https://doi.org/10.1117/12.2231925)
- Lage, C., Bradshaw, A., & Tyson, J. A. 2017, *Journal of Instrumentation*, 12, C03091, doi: [10.1088/1748-0221/12/03/C03091](https://doi.org/10.1088/1748-0221/12/03/C03091)



- Lesser, M., & Ouellette, D. 2017, *Journal of Instrumentation*, 12, C03080, doi: [10.1088/1748-0221/12/03/C03080](https://doi.org/10.1088/1748-0221/12/03/C03080)
- LSST Science Collaboration, Abell, P. A., Allison, J., et al. 2009, arXiv e-prints, arXiv:0912.0201, doi: [10.48550/arXiv.0912.0201](https://doi.org/10.48550/arXiv.0912.0201)
- Magnier, E. A., Tonry, J. L., Finkbeiner, D., et al. 2018, *PASP*, 130, 065002, doi: [10.1088/1538-3873/aaaad8](https://doi.org/10.1088/1538-3873/aaaad8)
- Mandelbaum, R. 2015, *Journal of Instrumentation*, 10, C05017, doi: [10.1088/1748-0221/10/05/C05017](https://doi.org/10.1088/1748-0221/10/05/C05017)
- Mandelbaum, R., Hirata, C. M., Seljak, U., et al. 2005, *MNRAS*, 361, 1287, doi: [10.1111/j.1365-2966.2005.09282.x](https://doi.org/10.1111/j.1365-2966.2005.09282.x)
- Meyers, J. E., & Burchat, P. R. 2015, *Journal of Instrumentation*, 10, C06004, doi: [10.1088/1748-0221/10/06/C06004](https://doi.org/10.1088/1748-0221/10/06/C06004)
- Miyazaki, S., Komiyama, Y., Kawanomoto, S., et al. 2018, *PASJ*, 70, S1, doi: [10.1093/pasj/psx063](https://doi.org/10.1093/pasj/psx063)
- Newbry, S., Lange, T., Roodman, A., et al. 2018, in *Society of Photo-Optical Instrumentation Engineers (SPIE) Conference Series*, Vol. 10702, *Ground-based and Airborne Instrumentation for Astronomy VII*, ed. C. J. Evans, L. Simard, & H. Takami, 1070258, doi: [10.1117/12.2314269](https://doi.org/10.1117/12.2314269)
- O'Connor, P., Antilogus, P., Doherty, P., et al. 2016, in *Society of Photo-Optical Instrumentation Engineers (SPIE) Conference Series*, Vol. 9915, *High Energy, Optical, and Infrared Detectors for Astronomy VII*, ed. A. D. Holland & J. Beletic, 99150X, doi: [10.1117/12.2232729](https://doi.org/10.1117/12.2232729)
- Okura, Y., Plazas, A. A., May, M., & Tamagawa, T. 2015, *Journal of Instrumentation*, 10, C08010, doi: [10.1088/1748-0221/10/08/C08010](https://doi.org/10.1088/1748-0221/10/08/C08010)
- Park, H., Nomerotski, A., & Tsybychev, D. 2017, *Journal of Instrumentation*, 12, C05015, doi: [10.1088/1748-0221/12/05/c05015](https://doi.org/10.1088/1748-0221/12/05/c05015)
- Park, H. Y., Karpov, S., Nomerotski, A., & Tsybychev, D. 2020, *Journal of Astronomical Telescopes, Instruments, and Systems*, 6, 1, doi: [10.1117/1.JATIS.6.1.011005](https://doi.org/10.1117/1.JATIS.6.1.011005)
- Plazas, A. A., Bernstein, G. M., & Sheldon, E. S. 2014a, *Journal of Instrumentation*, 9, C04001, doi: [10.1088/1748-0221/9/04/C04001](https://doi.org/10.1088/1748-0221/9/04/C04001)
- . 2014b, *PASP*, 126, 750, doi: [10.1086/677682](https://doi.org/10.1086/677682)
- Radeka, V. 2006, eConf, C0604032, 0005, <https://www.osti.gov/biblio/889288>
- Radeka, V., Frank, J., Geary, J. C., et al. 2009, *Journal of Instrumentation*, 03, 03002, doi: [10.1088/1748-0221/4/03/P03002](https://doi.org/10.1088/1748-0221/4/03/P03002)
- Roodman, A., Bogart, J. R., Bond, T., et al. 2018, in *Society of Photo-Optical Instrumentation Engineers (SPIE) Conference Series*, Vol. 10705, *Modeling, Systems Engineering, and Project Management for Astronomy VIII*, ed. G. Z. Angeli & P. Dierickx, 107050D, doi: [10.1117/12.2314017](https://doi.org/10.1117/12.2314017)
- Schneider, P. 2005, arXiv e-prints, astro, doi: [10.48550/arXiv.astro-ph/0509252](https://doi.org/10.48550/arXiv.astro-ph/0509252)
- Snyder, A., Gilmore, K., & Roodman, A. 2018, in *Society of Photo-Optical Instrumentation Engineers (SPIE) Conference Series*, Vol. 10709, *High Energy, Optical, and Infrared Detectors for Astronomy VIII*, ed. A. D. Holland & J. Beletic, 107092B, doi: [10.1117/12.2313875](https://doi.org/10.1117/12.2313875)
- Snyder, A., Longley, E., Lage, C., et al. 2021a, *Journal of Astronomical Telescopes, Instruments, and Systems*, 7, 048002, doi: [10.1117/1.JATIS.7.4.048002](https://doi.org/10.1117/1.JATIS.7.4.048002)
- Snyder, A., Barrau, A., Bradshaw, A., et al. 2021b, arXiv e-prints, arXiv:2101.01281, <https://arxiv.org/abs/2101.01281>
- Stubbs, C. W. 2014, *Journal of Instrumentation*, 9, C03032, doi: [10.1088/1748-0221/9/03/C03032](https://doi.org/10.1088/1748-0221/9/03/C03032)
- The LSST Dark Energy Science Collaboration, Mandelbaum, R., Eifler, T., et al. 2018a, arXiv e-prints, arXiv:1809.01669, doi: [10.48550/arXiv.1809.01669](https://doi.org/10.48550/arXiv.1809.01669)
- . 2018b, arXiv e-prints, arXiv:1809.01669, doi: [10.48550/arXiv.1809.01669](https://doi.org/10.48550/arXiv.1809.01669)

## APPENDIX

## A. OPERATION VOLTAGES

The LSSTCam operation voltages setups used during the data acquisitions are presented in [Table 2](#).

	e2v (Run 3)	e2v (Run 5)	ITL (Run 3)	ITL (Run 5)
Output Drain [V]	24.4	23.4	25.0	26.9
Reset Drain [V]	12.7	11.6	13.0	13.0
Guard Drain [V]	26.0	26.0	20.0	20.0
Output Gate [V]	-2.2	-3.4	-2.0	-2.0
Backbias [V]	-50.0	-50.0	-50.0	-50.0
Parallel Clock High [V]	3.4	3.3	2.0	2.0
Parallel Clock Low [V]	-5.8	-6.0	-8.0	-8.0
Serial Clock High [V]	4.7	3.9	5.0	5.0
Serial Clock Low [V]	-4.2	-5.4	-5.0	-5.0
Reset Gate High [V]	6.4	6.1	8.0	8.0
Reset Gate Low [V]	-3.4	-4.0	-2.0	-2.0
Gain	0	0	0	0
RC	3	14	3	14
sequencer file	FP_E2V_2s_ir2_v2.seq	FP_E2V_2s_ir2_v26.seq	FP_ITL_2s_ir2_v3.seq	FP_ITL_2s_ir2_v26.seq

**Table 2.** Nominal operational parameters for both e2v and ITL sensors in the different run campaigns for which we acquired spot projector data. See Figure 2 in [Snyder et al. \(2018\)](#) for the schematic diagram of voltages. RC and Gain are configurable settings in the readout electronics boards ([Juramy et al. 2014](#))

## B. SUPPLEMENTAL FIGURES

We show the figures 3, 4, and 5 for the other sensors studied: E2V - R24-S11 and R22-S11, and ITL - R10-S11 and R02-S02.

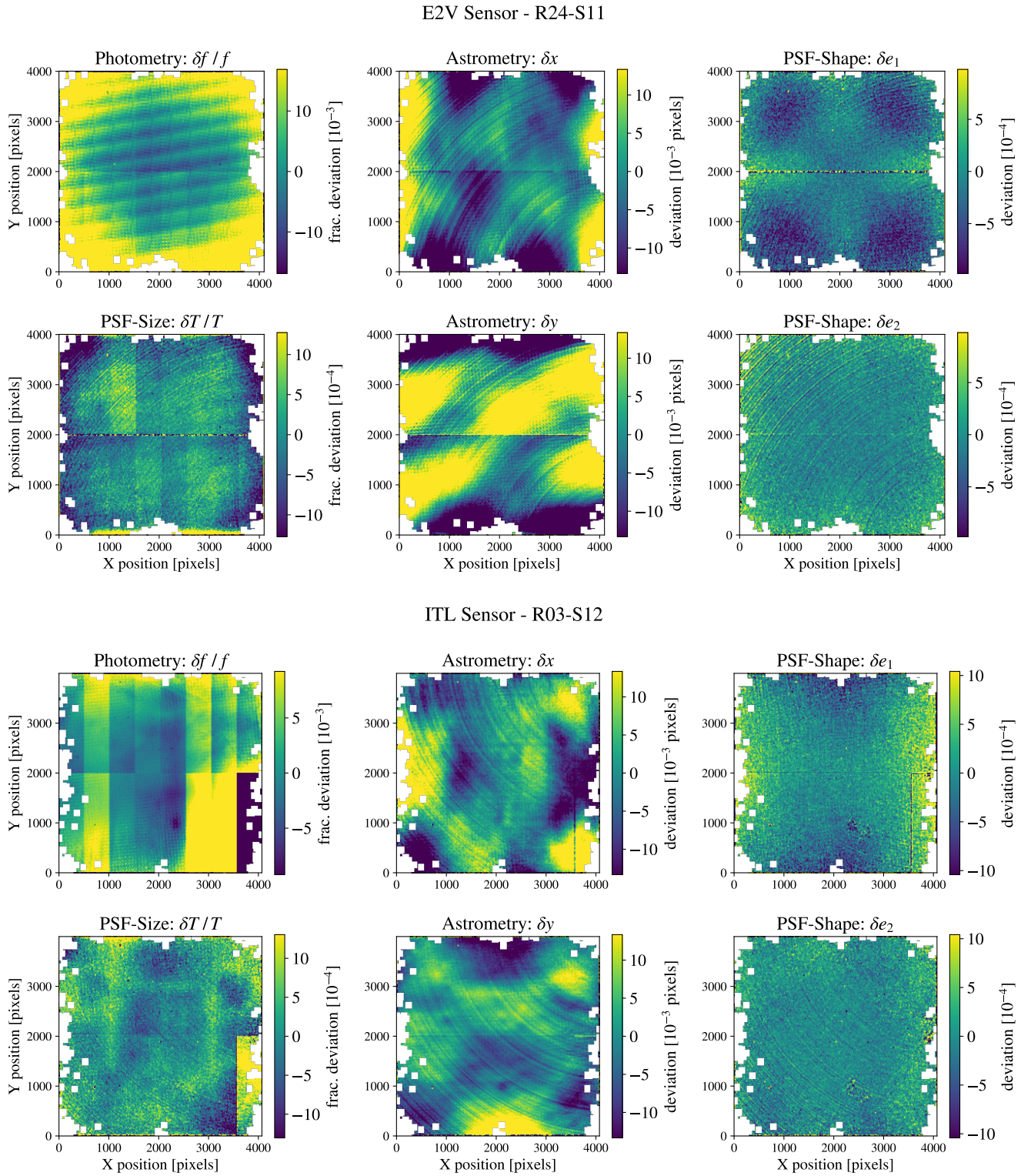


**Figure 7.** Same as Figure 3 caption. Note: the lower-right corner of R03-S12 is an image artifact, the spot images in this region are likely affected by stray light reflections from the side of the cryostat window.

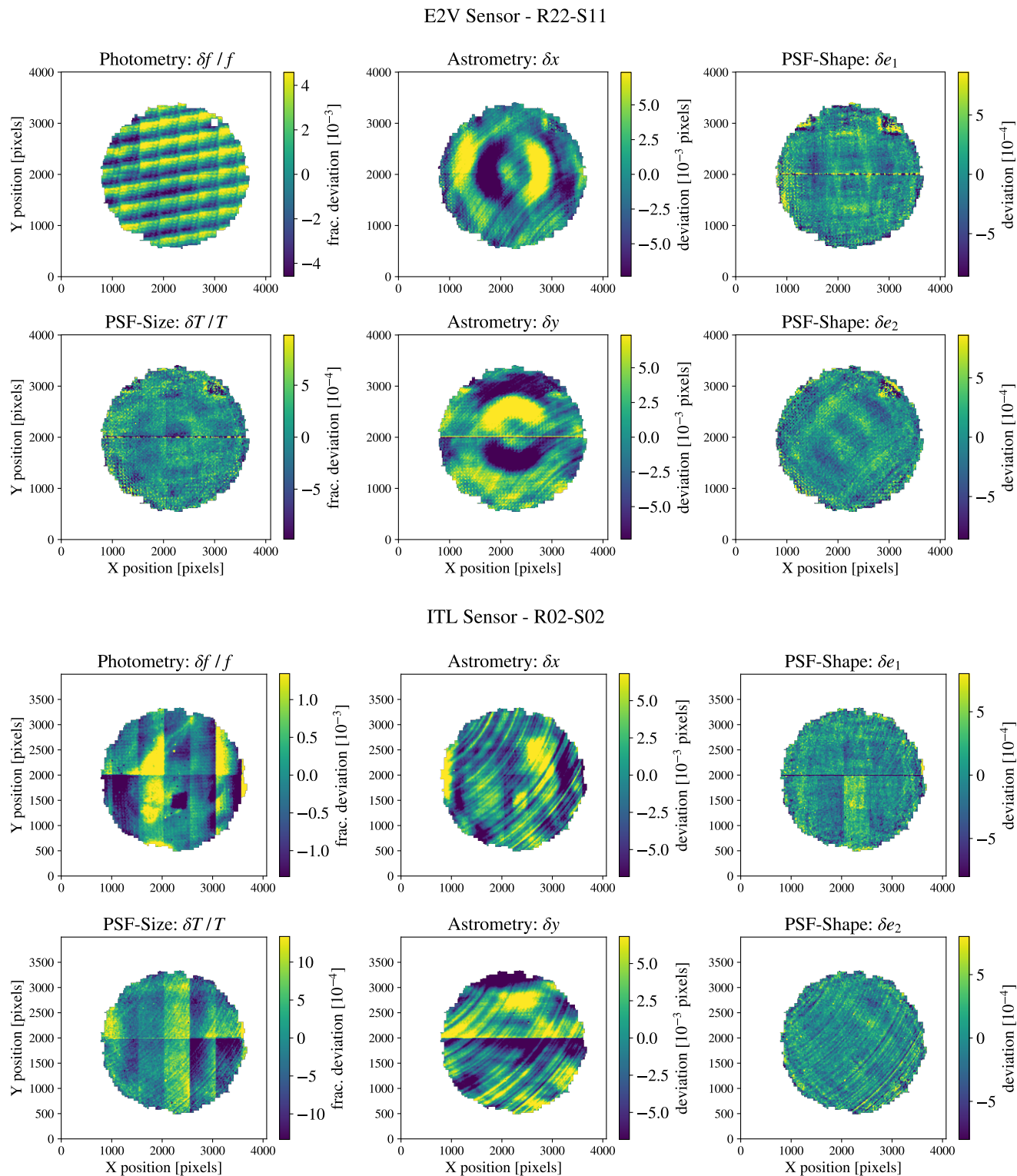


**Figure 8.** Same as Figure 3 caption. The data was collected during the Run 3 testing period. In this period the coverage of the fiducial spot projector position didn't extended to cover the entire CCD, which results in the circular shape map in the center of the CCD.



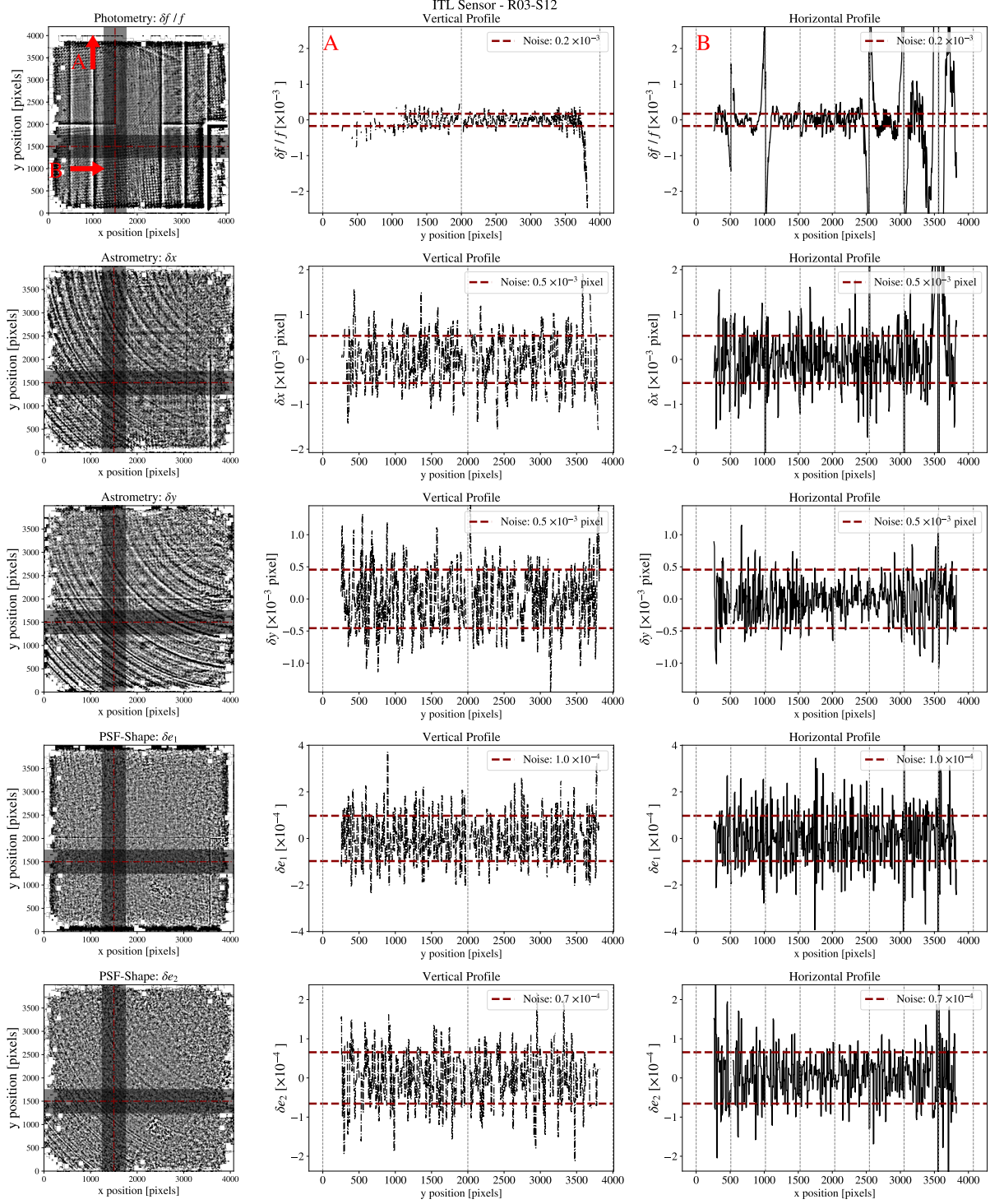


Figure 9. Same as Figure 4 caption.

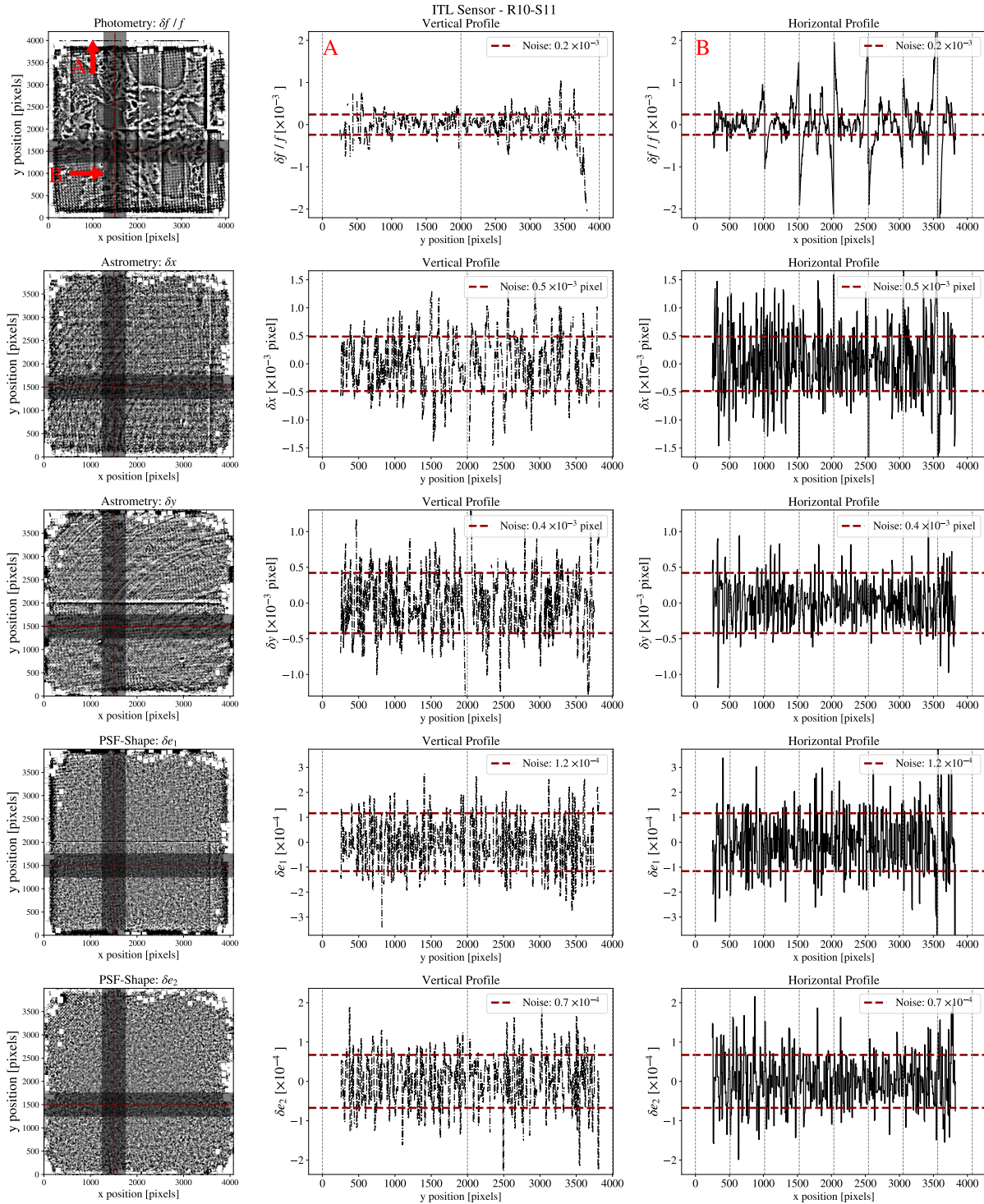


Figure 10. Same as Figure 4 caption.

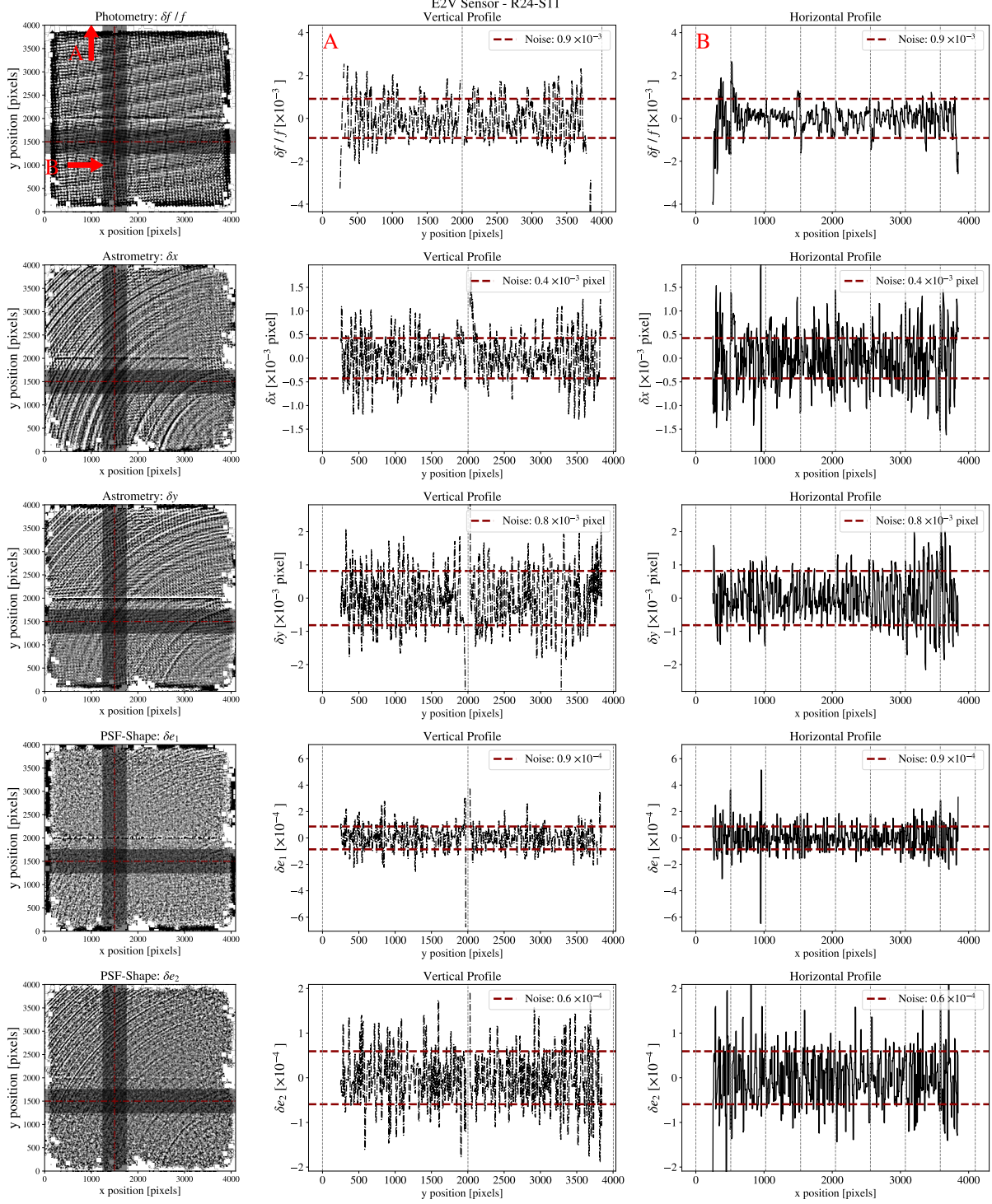


Figure 11. Same as Figure 4 caption.



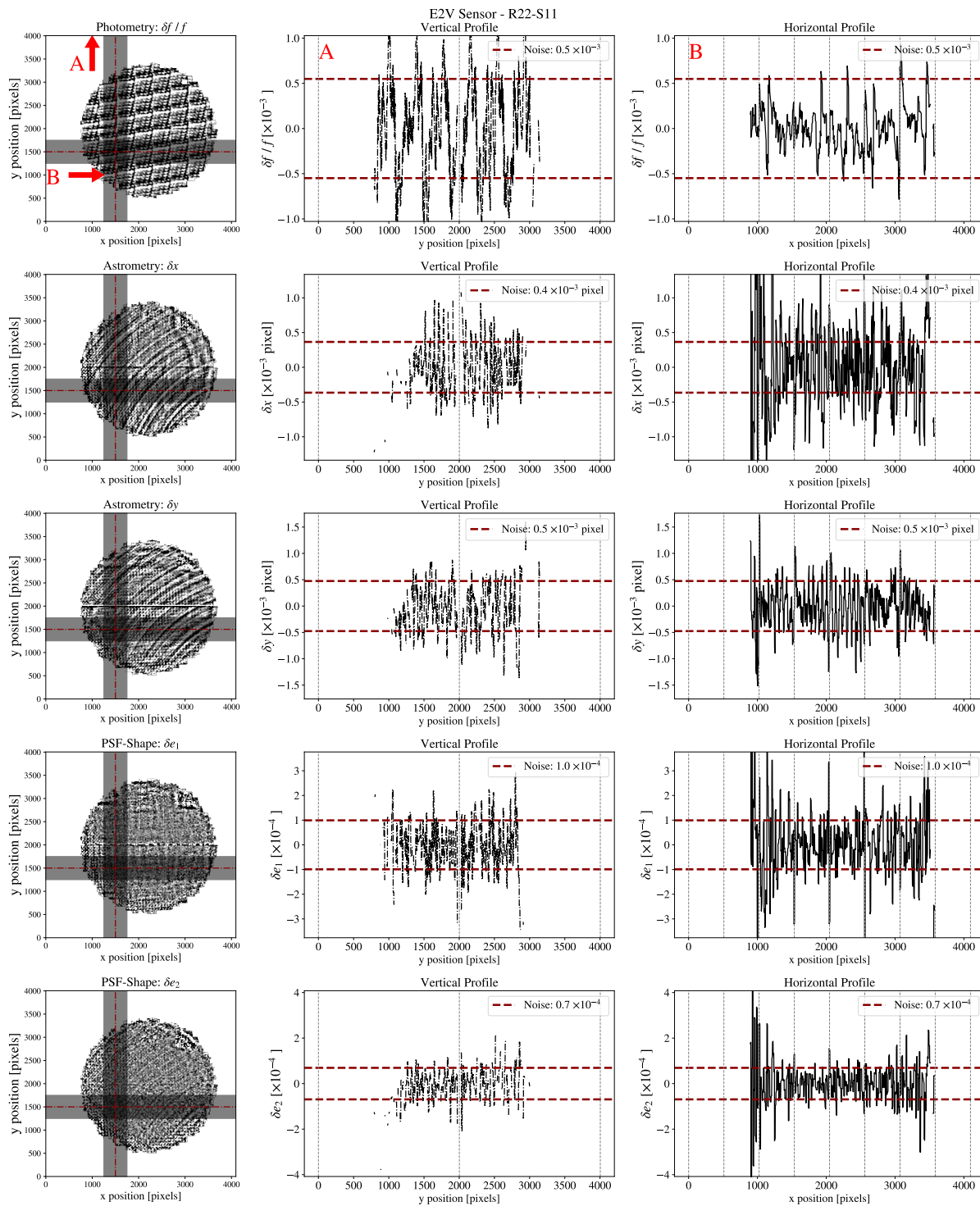


Figure 12. Same as Figure 4 caption. The data was collected during the Run 3 period.



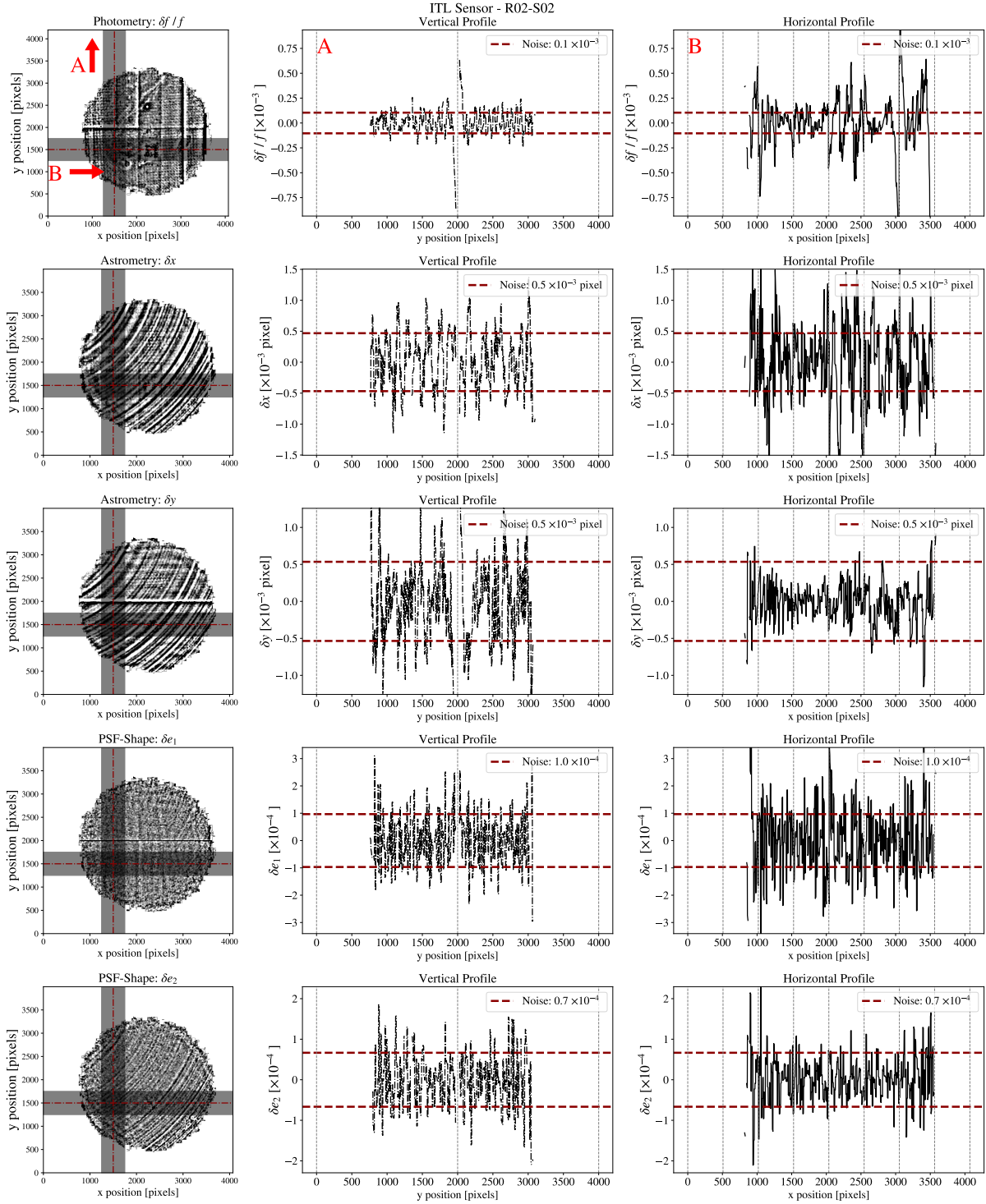


Figure 13. Same as Figure 4 caption. The data was collected during the Run 3 period.

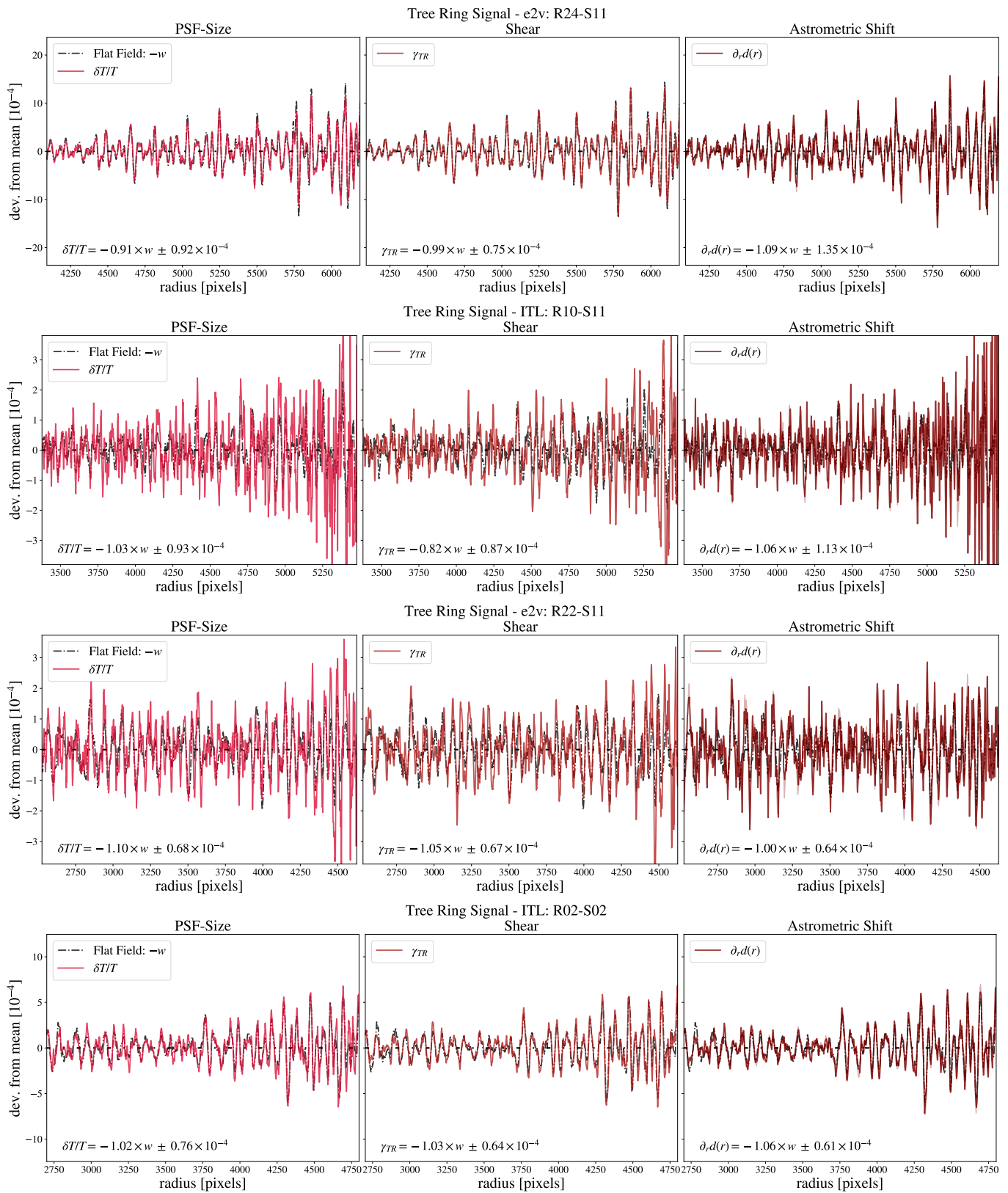


Figure 14. Same as Figure 5 caption.